3D ASSEMBLY FOR PROGRAMMABLE MATTER AND HOLLOW FIBER MEMBRANE GAS EXCHANGE IN PLANAR PHOTOBIOREACTORS

A Dissertation

Presented to the Faculty of the Graduate School

of Cornell University

In Partial Fulfillment of the Requirements for the Degree of

Doctor of Philosophy

by

Michael Kalontarov

January 2014

3D ASSEMBLY FOR PROGRAMMABLE MATTER AND
HOLLOW FIBER MEMBRANE GAS EXCHANGE IN PLANAR
PHOTOBIOREACTORS

Michael Kalontarov, Ph. D.
Cornell University 2014

In my Ph.D. research I have applied mechanical engineering knowledge and approaches to develop technologies for two topics: programmable matter and green energy through biofuels. Specifically, I have addressed the issues of 3D assembly in a fluid environment and gas exchange in photobioreactors. In the first part of this dissertation, I investigated a programmable matter system that consists of cm-scale building blocks which are agitated in a stochastic flow pattern and assembled using local fluid forces. The fundamental aspect of this approach that my research concentrated on was the problem of component alignment. Towards this end we developed a novel alignment strategy and characterized it using a combination of numerical simulations and experiments. In the second part of this dissertation, I demonstrate the optimal geometric and operational conditions for CO_2 transport to planar cultures of photosynthetic organisms via hollow fiber membranes. Firstly, I examined the growth pattern of *Synechococcus elongatus* around individual hollow fiber membranes to determine the optimal spacing and conditions for maximizing photosynthetic activity. I expanded on this initial work and used the information from the single fiber experiments to design, fabricate, and characterize arrays of HFM

fibers. By using this novel configuration of hollow fiber membranes, I was able to grow and sustain an organism culture with effectiveness comparable to state of the art methods while eliminating the need for media circulation and replenishment and allowing for integration into waveguide photobioreactors.

BIOGRAPHICAL SKETCH

Michael Kalontarov was born in 1985 and grew up in Dushanbe, Tajikistan, before immigrating to the United States in 1995. He attended Stuyvesant High School in New York City and completed his Bachelor of Engineering degree at the Department of Mechanical Engineering of the Cooper Union for the Advancement of Science and Art in 2007. For his graduate studies Michael joined the Erickson Lab at the Sibley School of Mechanical and Aerospace Engineering at Cornell University in 2007. During his tenure at the Erickson Lab, Michael contributed to several projects including "Programmable Matter" and "Advanced Photobiorefineries".

To my grandmother Iraida Kalontarova.

ACKNOWLEDGMENTS

First of all, I would like to thank Prof. Erickson, my PhD advisor and committee chair. His guidance and support have been invaluable in my efforts to complete my graduate studies. Though I did not initially start out in his lab and I am very glad that I joined the Erickson Lab in January of 2008. From Prof. Erickson's example I have learned a vast deal about work ethic, management, and leadership. Through good times and hard times, I can say that when I left his office at the end of our weekly meetings I always felt better about my research and progress than when I came in. I wish him the best of luck in his career and personal life.

I would like to thank the members of my committee Prof. Hod Lipson and Prof. Mason Peck. Their invaluable feedback and guidance have assisted me in my pursuit of a doctorate.

I am also very grateful that I became a member of the Erickson lab because there I got to work with some brilliant people who were my colleagues and also my friends. I would like to thank my teammates on the ARPA-E project for all of their help and support: Devin Doud, Erica Jung, Aadhar Jain, Saad Ahsan, Erik Bland, and Nina Voulis. I especially want to thank Devin who has been providing me with batches of fresh bacteria for many years and Erica who has been on the project from the start. I would like to thank Michael Mak, Xavier Serey, Pilgyu Kang, Li Jiang, Vlad-Victor Oncescu, Seoho Lee, Dakota O'Dell, and Perry Schein, for being easy and fun to work and talk with. I would be remiss if I did not thank the alumni of our lab for their great guidance, support, and friendship when I was a new member, most notably Bernardo

Cordovez, Aram Chung, and Mekala Krishnan. Last but not least, I would like to thank Matthew Mancuso for sharing lunch and coffee breaks with me over the last several years; our talks have been a tremendous help and inspiration for me, and I wish him all of the best in his future endeavors.

Over the last six years I have been away from home, but I have always felt my family's support and love. My parents and grandparents went through a lot to allow me to have this opportunity. During the course of my studies I appreciated their phone calls and concern, and the fact that every trip home felt like a small vacation and holiday. I would also like to thank my sister and cousins for their support and care, and for making the trips to visit me in Ithaca. Most importantly, I am grateful that my grandmother Iraida knew that the day of my defense was set and that I knew how glad and proud she was at hearing that news.

TABLE OF CONTENTS

LIST OF FIGURES

LIST OF TABLES

LIST OF SYMBOLS

$\mathbf{u}$ = velocity of the fluid

ρ = fluid density

p = pressure

v = viscosity

F = force on block

$\mathbf{T_B}$ = torque on block

$\boldsymbol{\tau}$ **=** fluid stress tensor.

θ = initial polar angle between the block and a normal to the docking site

φ = initial clockwise angle of rotation of the block

CHAPTER 1

INTRODUCTION

1.1 3D Fluidic Assembly for Programmable Matter

Programmable matter is concept which is easily imagined by science fiction writers and movie directors. One such writer has described a world in which this technology has been implemented: “4 July 2100. The flick of a switch: a wall becomes a window becomes a door. Any chair becomes a hyper-computer, any rooftop a power or waste-treatment plant.” [1]. The freedom of function and design that such control of the properties of any object would grant us would fundamentally change how we interact with our world. There are many ways in which the implementation of such as system can be imagined, from the manipulation of DNA strands [2] to miniature robots [3]. One fundamental way to approach actualizing such as system is to design and fabricate a set of building blocks which can be assembled, disassembled, and reassembled into various objects or devices. Such devices would be very robust and have multifaceted uses due to their ability to change their shape and physical properties and therefore their function. This approach is quite different from traditional manufacturing where many tools have been developed to fabricate devices to address specific needs and applications. This means that the devices have limited capability to change when new applications come up, and it is easier to design and fabricate new devices when such situations arise. In contrast, a programmable system would involve only one initial design and fabrication step, which would be the

manufacturing of the building blocks. The system could adapt to any new applications by rearranging these blocks. Such robustness and reconfigurability could be put to great use in robotics, defense, and exploration.The goal of the research in this field is to develop assembly methods that can manipulate large numbers of building blocks in parallel manner to form useful structures. Though a fully implemented system would involve interactions on all length scales, initial research approaches could be classified by such a metric.

At the micro- and nanoscales, researchers have explored fluidic self-assembly for this application. Lithographically directed self-assembly has been used to assemble nanoscale structures[4]. Various microscale devices have been self-assembled from multiple parts using fluid and capillary force driven processes [5-7]. Capillary forces can also be used for directed self-assembly by controlling binding affinities at interaction sites using electrical [8] or thermal fields [9]. These techniques have taken a programmable matter approach to the fabrication of complex Micro-Electro-Mechanical System (MEMS) devices [10], focusing on forming functional units instead of assembling structures.

Other systems have been developed that allow for the programmable assembly of structures. A microfluidic rail network has been demonstrated as a platform for the assembly of structures from polymer component [11]. Though successful at assembling many structural forms by manipulating many components in parallel, the system required the fabrication of a new unique rail network to assemble new structures. Another approach for programmable assembly of non-predetermined

structures has been demonstrated by manipulating fluid flow in an unstructured microfluidic chamber [12, 13]. The architecture of this assembler is independent of the target structure, and only the actuation of the valves controlling the flow has to be reprogrammed.

Though many advances in programmable assembly have been made at the small scale, they are limited to a 2D space and have limited applicability to the macroscopic world. An extra degree of freedom that that is available at the microscale is that the building blocks can be self-propelled instead of driven by external forces [14]. These types of systems have been explored in the context of reconfigurable [15] and modular robotics [16]. Though this feature adds extra functionality to the building blocks and could be very promising in the future, the high power requirements and limited three-dimensional mobility constrain the application of these systems for now. Externally driven systems have been developed and explored self-replication in 1D [17] and 2D [18]. 2D macroscale programmable assembly systems have demonstrated assembly of shapes[19] and self-reconfiguration[20]. The limiting factor keeping these systems confined to 2D is the method of agitation. One way to avoid this issue is too start with a pre-assembled 3D lattice of building blocks and selectively disassemble the lattice to shape the desired final structure [21]. Though this approach is very good for achieving a desired structure and 3D assembly technique still needs to be developed to reform the original lattice. A more direct approach is to design a system for 3D agitation of the building blocks. Such a system has been tested with 10-cm scale components and has shown promising results [22], and investigate using numerical simulations [23]. The system consists of a large fluid filled chamber in which the components can float

and the flow is agitated by recirculating the fluid in the chamber. However, the large size of the components is too far from the resolution that is desired for a programmable matter system. In my work, I have attempted to bridge this gap by working with mesoscale building blocks whose characteristic dimension is about a centimeter.

The approach to programmable matter that was investigated in my work is called 3D Fluidic Assembly, and it is illustrated in chapter 2. This system consists of cm-scale building blocks that are agitated in a stochastic flow pattern and assembled using local fluid forces. The fundamental aspect of this approach that my research concentrated on was the problem of component alignment. This problem was investigated using a combination of numerical simulations and experiments. Numerical simulations were conducted in order to study how blocks approach a sink in a stagnant flow to gain insight into dealing with the degrees of freedom in the system. The numerical results were used to design blocks for experiments in a prototype assembly chamber. These experiments also allowed us to develop strategies for alignment.

1.2 Hollow fiber membrane arrays for gas exchange in photobioreactors

As a society we have recently become increasingly concerned with problems of energy security, CO_2 emissions, and climate change [24]. These three concerns could be addressed by switching to alternative energy sources. Though electrical power can be produced by many means there will still be a need for the production of a

renewable and sustainable liquid fuel. Biofuel production is an approach that can satisfy these requirements [25]. The production of these fuels takes advantage of a fundamental property of photoautotrophic organisms: fixation of inorganic carbon (CO_2) into useful biomolecules using energy from sunlight [26]. The first generation organisms used for this purpose have been plant crops. Though biofuel production using higher plants, such as corn or sugarcane, has been already been implemented it has disadvantages in terms of carbon efficiency and land use [27]. Additionally, pressure has been put on the food supply as these plants compete for land use with traditional agriculture [28]. Cyanobacteria and microalgae have been suggested as a better class of organisms for this purpose. These organisms have higher CO_2 fixation efficiencies and growth rates than plant crops and the potential to utilize waste-water or industrial gas wastes as nutrient sources [29].

The utilization of these organisms for fuel production is limited by two factors: harvesting of the fuel product after organism cultivation and the efficiency of the photobioreactors (PBRs) where these organisms a cultivated. The most widely implemented method for fuel production from microalgae is biodiesel [30]. This involves cultivating the microorganism to a sufficient biomass and then extracting the stored lipids from the cells. However, this is very energy intensive and contributes to the overall inefficiency and cost of the system [31]. One approach to mitigating this problem is to use of engineered strains of cyanobacteria that have the ability to directly secrete fuels. For example, bacteria strains that directly secrete hydrogen [32, 33], ethanol [34, 35], isobutyraldehyde [36] and other high value products [37] been reported.

To take advantage of the capabilities of these strains, efficient PBRs have to be developed. The goal of a PBR is to deliver light, inorganic carbon (chiefly in the form of CO_2), allow for the exchange of O_2, and the extraction of the fuel product [38]. The most developed reactors are open raceway ponds and tubular-type enclosed reactors [39]. These technologies offer many advantages but they are limited in the amount of fuel that they can produce since they do not efficiently perform the goals mentioned above [40].

Addressing the goal is the maximization of the light utilization in PBRs has long been a crucial concern in PBR development [38]. As the density of the mass algal culture increases, self-shading by the algae limits the penetration depth of useful quantities of light. This causes the culture to be overexposed at the surface and underexposed below the penetration depth [41]. A new approach for PBR development, wherein photonic structures are used to improve the light distribution, has been proposed as way forward for cultivating high density cultures in compact volumes [42]. Further work has been done to explore the interaction of photosynthetic bacteria with photonic phenomenon such as evanescent [43] and plasmonic fields [44]. As a co-author, I have contributed to experiments that have demonstrated the ability to grow bacteria on a slab waveguide, which can be stacked to create a scalable light delivery system [45].

My contribution as first author has dealt with the goal of efficient gas exchange in PBRS. Currently employed methods for gas exchange include the aeration of the growth media by exposure to the atmosphere and bubbling [46]. It is challenging to

maintain a uniform distribution of CO_2 using these methods [47], and this is important for efficient volume utilization since regions with low CO_2 concentration suffer from lower rates of photosynthesis [48]. It is also necessary to remove O_2 from the growth media as it accumulates there as a byproduct of photosynthesis, and over time inhibits the photosynthetic machinery [38]. Keeping the concentrations of these species at the proper levels requires high mixing rates, which consumes a large amount of energy [49], and contributes to the already high energy costs of the algal cultivation process [50]. A technology that has been recently advanced as a way to improve PBR gas exchange are hollow fiber membranes (HFMs).

Hollow fiber membranes consist of hollow porous fibers that serve as the membrane and allow for diffusive species exchange between the fiber lumen and the external media. They are usually deployed in modules and have been used in a large variety of applications including wastewater [51], landfill [52] and drinking water treatment [53], tissue engineering [54], and the development of artificial organs[55]. Since HFM gas exchange is driven by the partial pressures differences across the membrane they allow for both CO_2 delivery and O_2 removal [56, 57]. In addition, another potential advantage is the ability to extract soluble products using compatible HFMs. HFM modules have been incorporated into laboratory scale PBRs with a range of cyanobacteria and microalgae. The results of these studies have verified the potential benefits of integration of HFMs into PBRs by reporting increased biomass production, improved gas exchange, regulation of pH, and promotion of CO_2 [57-60].

Though the use of HFM modules has shown promise, the PBRs investigated in those experiments use direct illumination to deliver light into the reactor. In contrast, my work has concentrated on integrating the benefits of HFM gas exchange with those of planar guided light delivery that has been developed in our lab [45]. In a planar waveguide system circulation is limited, due to the close proximity of the light guiding elements, and so the HFM have to be applied directly, as opposed to in a module. Distributing the HFM fibers through the reactor has analogous advantages to guiding light through the reactor using photonic elements. The fibers provide both a pathway for CO_2 to be delivered deep into the reactor and also allow for O_2 and products to be removed. Additionally, by properly distributing the fibers we can ensure a uniform distribution of CO_2 and achieve complete volume utilization.

In order to achieve these aims, I first conducted experiments with a single HFM fiber. The results of this work are presented in Chapter 3. Miniature reactors with only one HFM fiber were fabricated to investigate the effect on photosynthetic bacteria growth the fiber had in its micro-environment. We characterized this by studying the growth of *S. elongatus* in CO_2 limited conditions where the HFM fiber served as the only CO_2 source. Changes in the bacterial distribution as a function of time for several initial bacteria concentrations were characterized and compared to controls. In Chapter 4, I expanded on this initial work and used the information from the single fiber experiments to design, fabricate, and characterize the geometric and operation conditions for an array of HFM fibers. We report on three experiments that investigate the effects of inter-fibre spacing and active/passive aeration on the organism growth rate, planar surface density, and total biomass accumulation. First, we have

characterized what array spacing might be most effective by studying a two fiber unit cell. We then fabricated full HFM arrays and measured the behavior of the organisms for an extended period of time (30 days). Lastly, a study characterizing the effect of adding active gas flow through the fibers was conducted.

1.3 Research Overview and Dissertation Breakdown

In Chapter 2, I present a method for fluid dynamically driven assembly in three dimensions and demonstrate its applicability to the development of programmable matter. Briefly, I investigate docking of a single block onto a larger structure using detailed numerical simulations and experiments. The simulation results show that a block whose degrees of freedom are limited is able to align parallel with the docking site, leading to successful assembly whereas unconfined blocks were not. Experiments with blocks that were designed with this approach confirmed alignment parallel with the docking site in 97% of trials. To generate alignment in the other two planes, I developed blocks that self-align due to geometric interactions and introduced a pulsating flow to increase the probability of aligned assembly. Using this strategy, a 54% successful (fully aligned) assembly rate was achieved.

In Chapter 3, I present the results of our first investigation of the applicability of HFMs for PBR gas exchange. Recently, cyanobacteria have been metabolically engineered to secrete valuable biofuel precursors eliminating the requirement to harvest and post-process algal biomass. However, development of new PBRs that can efficiently deliver light and address the mass transport challenges associated with maintaining high cyanobacteria productivity has been lagging. HFMs are a method for

bubble-less gas exchange that has been shown to be effective at enhancing mass transfer. Previous applications of HFM technology to PBRs have been limited to exploring its ability to enhance CO_2 delivery to the bulk liquid volume. To investigate potential strategies for novel PBR design configurations, I examined the growth pattern of *Synechococcus elongatus* around individual hollow fiber membranes to determine the optimal spacing and conditions for maximizing photosynthetic activity. I have shown that a single fiber enabling passive transport from/to the atmosphere can provide enough gas exchange to increase biomass accumulation by > 2.5 times with respect to a non-fiber control. This increased growth was found to decay in the radial direction with the enhanced growth area spanning between 1.2 mm and 1.7 mm depending on the initial inoculation concentration.

In Chapter 4, I present the results of our investigation HFM arrays. Here I demonstrate the optimal geometric and operational conditions for CO_2 transport to planar cultures of photosynthetic organisms via hollow fiber membrane arrays. Specifically I investigate the effects inter-fiber spacing and active/passive aeration on the organism growth rate, planar surface density, and total biomass accumulation. I show that spacing larger than 3 times the fiber diameter lead to significant variations in the surface density and spatially resolved growth rate, whereas at around this spacing culture densities nearing 90% can be maintained for 17 days without decrease. Active aeration was shown to increase the specific growth rate and the average surface density by approximately 15% and 35%, respectively, while also eliminating gradients in the growth rate along the length of the fibers.

REFERENCES

1. McCarthy, W., *Programmable matter.* Nature, 2000. **407**(6804): p. 569-569.
2. Seeman, N.C., *DNA in a material world.* Nature, 2003. **421**(6921): p. 427-431.
3. Cheung, K.C., et al., *Programmable Assembly With Universally Foldable Strings (Moteins).* Robotics, IEEE Transactions on, 2011. **27**(4): p. 718-729.
4. Liddle, J.A., Y. Cui, and P. Alivisatos, *Lithographically directed self-assembly of nanostructures.* Journal of Vacuum Science & Technology B, 2004. **22**(6): p. 3409-3414.
5. Srinivasan, U., D. Liepmann, and R.T. Howe, *Microstructure to substrate self-assembly using capillary forces.* Journal of Microelectromechanical Systems, 2001. **10**(1): p. 17-24.
6. Avital, A. and E. Zussman, *Fluidic assembly of optical components.* IEEE Transactions on Advanced Packaging, 2006. **29**(4): p. 719-724.
7. Morris, C.J. and B.A. Parviz, *Self-assembly and characterization of Marangoni microfluidic actuators.* Journal of Micromechanics and Microengineering, 2006. **16**(5): p. 972-980.
8. Chung, J.H., et al., *Programmable reconfigurable self-assembly: Parallel heterogeneous integration of chip-scale components on planar and nonplanar surfaces.* Journal of Microelectromechanical Systems, 2006. **15**(3): p. 457-464.

9. Sharma, R., *Thermally controlled fluidic self-assembly.* Langmuir, 2007. **23**(12): p. 6843-6849.

10. Mastrangeli, M., et al., *Self-assembly from milli-to nanoscales: methods and applications.* Journal of Micromechanics and Microengineering, 2009. **19**(8): p. 1-37.

11. Chung, S.E., et al., *Guided and fluidic self-assembly of microstructures using railed microfluidic channels.* Nature Materials, 2008. **7**(7): p. 581-587.

12. Tolley, M.T., et al., *Dynamically programmable fluidic assembly.* Applied Physics Letters, 2008. **93**(25).

13. Krishnan, M., et al., *Increased robustness for fluidic self-assembly.* Physics of Fluids, 2008. **20**(7).

14. Gross, R. and M. Dorigo, *Self-assembly at the macroscopic scale.* Proceedings of the IEEE, 2008. **96**(9): p. 1490-1508.

15. Castano, A., A. Behar, and P.M. Will, *The Conro modules for reconfigurable robots.* IEEE-ASME Transactions on Mechatronics, 2002. **7**(4): p. 403-409.

16. Dorigo, M., et al., *Evolving self-organizing behaviors for a swarm-bot.* Autonomous Robots, 2004. **17**(2-3): p. 223-245.

17. Penrose, L.S. and R. Penrose, *Self-Reproducing Analogue.* Nature, 1957. **179**(4571): p. 1183-1183.

18. Griffith, S., D. Goldwater, and J.M. Jacobson, *Robotics - Self-replication from random parts.* Nature, 2005. **437**(7059): p. 636-636.

19. Klavins, E., *Programmable Self-assembly.* IEEE Control Systems Magazine, 2007. **27**(4): p. 43-56.

20. White, P.J., K. Kopanski, and H. Lipson. *Stochastic self-reconfigurable cellular robotics*. in *Proc. 2004 IEEE Int. Conf. Robot. Autom.* 2004. Los Alomitos, CA.

21. Gilpin, K., et al., *Miche: Modular shape formation by self-disassembly.* International Journal of Robotics Research, 2008. **27**(3-4): p. 345-372.

22. White, P., et al. *Three Dimensional Stochastic Reconfiguration of Modular Robots*. in *Proceedings of Robotics Science and Systems*. 2005. MIT.

23. Tolley, M.T., et al., *Stochastic Modular Robotic Systems: A Study of Fluidic Assembly Strategies.* Robotics, IEEE Transactions on, 2010. **26**(3): p. 518-530.

24. Lam, M.K., K.T. Lee, and A.R. Mohamed, *Current status and challenges on microalgae-based carbon capture.* International Journal of Greenhouse Gas Control, 2012. **10**: p. 456-469.

25. Sheridan, C., *Making green.* Nature Biotechnology, 2009. **27**(12): p. 1074-1076.

26. Brennan, L. and P. Owende, *Biofuels from microalgae-A review of technologies for production, processing, and extractions of biofuels and co-products.* Renewable & Sustainable Energy Reviews, 2010. **14**(2): p. 557-577.

27. Searchinger, T., et al., *Use of US croplands for biofuels increases greenhouse gases through emissions from land-use change.* Science, 2008. **319**(5867): p. 1238-1240.

28. Fargione, J., et al., *Land clearing and the biofuel carbon debt.* Science, 2008. **319**(5867): p. 1235-1238.

29. Williams, P.J.L., *Biofuel: microalgae cut the social and ecological costs.* Nature, 2007. **450**(7169): p. 478-478.

30. Chisti, Y., *Biodiesel from microalgae.* Biotechnology Advances, 2007. **25**(3): p. 294-306.

31. Sander, K. and G.S. Murthy, *Life cycle analysis of algae biodiesel.* International Journal of Life Cycle Assessment, 2010. **15**(7): p. 704-714.

32. Ghirardi, M.L., et al., *Hydrogenases and hydrogen photoproduction in oxygenic photosynthetic organisms*, in *Annual Review of Plant Biology*2007. p. 71-91.

33. McNeely, K., et al., *Redirecting Reductant Flux into Hydrogen Production via Metabolic Engineering of Fermentative Carbon Metabolism in a Cyanobacterium.* Applied and Environmental Microbiology, 2010. **76**(15): p. 5032-5038.

34. Deng, M.D. and J.R. Coleman, *Ethanol synthesis by genetic engineering in cyanobacteria.* Applied and Environmental Microbiology, 1999. **65**(2): p. 523-528.

35. Luo, D.X., et al., *Life Cycle Energy and Greenhouse Gas Emissions for an Ethanol Production Process Based on Blue-Green Algae.* Environmental Science & Technology, 2010. **44**(22): p. 8670-8677.

36. Atsumi, S., W. Higashide, and J.C. Liao, *Direct photosynthetic recycling of carbon dioxide to isobutyraldehyde.* Nature Biotechnology, 2009. **27**(12): p. 1177-U142.

37. Ducat, D.C., J.C. Way, and P.A. Silver, *Engineering cyanobacteria to generate high-value products.* Trends in Biotechnology, 2011. **29**(2): p. 95-103.

38. Williams, P.J.L. and L.M.L. Laurens, *Microalgae as biodiesel & biomass feedstocks: Review & analysis of the biochemistry, energetics & economics.* Energy & Environmental Science, 2010. **3**(5): p. 554-590.

39. Aitken, D. and B. Antizar-Ladislao, *Achieving a Green Solution: Limitations and Focus Points for Sustainable Algal Fuels.* Energies, 2012. **5**(5): p. 1613-1647.

40. Xu, L., et al., *Microalgal bioreactors: Challenges and opportunities.* Engineering in Life Sciences, 2009. **9**(3): p. 178-189.

41. Lee, C.G., *Calculation of light penetration depth in photobioreactors.* Biotechnol. Bioprocess Eng., 1999. **4**: p. 78-81.

42. Erickson, D., D. Sinton, and D. Psaltis, *Optofluidics for energy applications.* Nature Photonics, 2011. **5**(10): p. 583-590.

43. Ooms, M.D., et al., *Evanescent photosynthesis: exciting cyanobacteria in a surface-confined light field.* Physical Chemistry Chemical Physics, 2012. **14**(14): p. 4817-4823.

44. Ooms, M.D., L. Bajin, and D. Sinton, *Culturing photosynthetic bacteria through surface plasmon resonance.* Applied Physics Letters, 2012. **101**(25).

45. Jung, E.E., et al., *Slab waveguide photobioreactors for microalgae based biofuel production.* Lab on a Chip, 2012. **12**(19): p. 3740-3745.

46. Kumar, A., et al., *Enhanced CO(2) fixation and biofuel production via microalgae: recent developments and future directions.* Trends in Biotechnology, 2010. **28**(7): p. 371-380.

47. Carvalho, A.P. and F.X. Malcata, *Transfer of carbon dioxide within cultures of microalgae: Plain bubbling versus hollow-fiber modules.* Biotechnology Progress, 2001. **17**(2): p. 265-272.

48. Sanchez, G.B., M; Rodriguez, F; Sevilla, FJM; Alias, BC; Fernandez, AFC., *Minimization of carbon losses in pilot-scale outdoor photobioreactors by model-based predictive control.* Biotechnol Bioeng., 2003. **84**(5): p. 532-43

49. Beal, C.M., et al., *The Energy Return on Investment for Algal Biocrude: Results for a Research Production Facility.* Bioenergy Research, 2012. **5**(2): p. 341-362.

50. Chisti, Y., *Response to Reijnders: Do biofuels from microalgae beat biofuels from terrestrial plants?* Trends in Biotechnology, 2008. **26**(7): p. 351-352.

51. Agrahari, G.K., et al., *Removal of dissolved H2S from wastewater using hollow fiber membrane contactor: Experimental and mathematical analysis.* Desalination, 2013. **314**: p. 34-42.

52. Ahmed, F.N. and C.Q. Lan, *Treatment of landfill leachate using membrane bioreactors: A review.* Desalination, 2012. **287**: p. 41-54.

53. De Souza, N.P. and O.D. Basu, *Comparative analysis of physical cleaning operations for fouling control of hollow fiber membranes in drinking water treatment.* Journal of Membrane Science, 2013. **436**: p. 28-35.

54. Mohebbi-Kalhori, D., et al., *Computational modeling of adherent cell growth in a hollow-fiber membrane bioreactor for large-scale 3-D bone tissue engineering.* Journal of Artificial Organs, 2012. **15**(3): p. 250-265.

55. Palakkan, A.A., et al., *Evaluation of Polypropylene Hollow-Fiber Prototype Bioreactor for Bioartificial Liver.* Tissue Engineering Part A, 2013. **19**(9-10): p. 1056-1066.

56. Gabelman, A. and S.T. Hwang, *Hollow fiber membrane contactors.* Journal of Membrane Science, 1999. **159**(1-2): p. 61-106.

57. Fan, L.H., et al., *Optimization of carbon dioxide fixation by Chlorelia vulgaris cultivated in a membrane-photobioreactor.* Chemical Engineering & Technology, 2007. **30**(8): p. 1094-1099.

58. Fan, L.-H., et al., *Evaluation of a membrane-sparged helical tubular photobioreactor for carbon dioxide biofixation by Chlorella vulgaris.* Journal of Membrane Science, 2008. **325**(1): p. 336-345.

59. Kim, H.W., et al., *Advanced Control for Photoautotrophic Growth and CO(2)-Utilization Efficiency Using a Membrane Carbonation Photobioreactor (MCPBR).* Environmental Science & Technology, 2011. **45**(11): p. 5032-5038.

60. Kumar, A., et al., *A hollow fiber membrane photo-bioreactor for CO(2) sequestration from combustion gas coupled with wastewater treatment: A process engineering approach.* Journal of Chemical Technology and Biotechnology, 2010. **85**(3): p. 387-394.

CHAPTER 2

HYDRODYNAMICALLY DRIVEN DOCKING OF BLOCKS FOR 3D FLUIDIC ASSEMBLY

2.1 Abstract

In this work we develop a method for fluid dynamically driven assembly in three dimensions and demonstrate its applicability to the development of programmable matter. Towards this end we investigate docking of a single block onto a larger structure using detailed numerical simulations and experiments. Our simulation results show that a block whose degrees of freedom are limited is able to align parallel with the docking site leading to successful assembly whereas unconfined blocks were not. Experiments with blocks that were designed with this approach confirmed alignment parallel with the docking site in 97% of trials. To generate alignment in the other two planes, we designed blocks that self-align due to geometric interactions. We also introduced a pulsating flow to increase the probability of aligned assembly. Using this strategy, a 54% successful (fully aligned) assembly rate was achieved.

*Reprinted by permission of the Springer-Verlag with permission from Michael Kalontarov, Michael T. Tolley, Hod Lipson, and David Erickson, "Hydrodynamically driven docking of blocks for 3D fluidic assembly", *Microfluidics and Nanofluidics*, 2010. **9**(2-3): p. 551-558, http://dx.doi.org/10.1007/s10404-010-0572-9 © Springer-Link

2.2 Introduction

Programmable matter is concept by which objects or devices are constructed from a set of fundamental building blocks that can be automatically assembled, dissembled, and reassembled into various functional forms capable of performing different tasks. Traditional manufacturing techniques are well suited to create devices designed for specific, pre-determined uses. When a new capability is desired or required, via these methods it is often easier to construct an entirely new device rather than try to reconfigure the old one. In an ideal programmable matter system the building blocks only need to be manufactured once and reconfiguration could be done automatically in response to changing needs. The development of such a system would have wide application in robotics, defense, and exploration.

The eventual attainment of such a system requires the development of new assembly methods that can reversibly bring together large numbers of building blocks in a highly parallel manner. At the micro- and nanoscales, fluidic self-assembly is an approach by which this could be achieved. Nano-scale structures have been assembled using lithographically directed self-assembly [1]. At the microscale, fluid and capillary driven self-assembly of microscale actuators, electrical and optical components has been demonstrated [2-4]. Directed self-assembly of microparts has been approached by thermally [5] and electrically [6] controlling the binding affinities of capillary force interaction sites. These techniques are useful for the assembly of complex Micro-Electro-Mechanical System (MEMS) devices because they allow large numbers of components that are made by different processes to be integrated in a highly parallel manner [7]. Other systems have been developed that allow for the programmable

assembly of structures. Chung *et al.* [8] for example demonstrated a system which utilizes a microfluidic rail networks to assemble a wide range of micro-structures from polymer components. However, a new and specific microfluidic rail network needs to be constructed for every assembly task. Tolley *et al.* [9] and Krishnan *et al.* [10] demonstrated the directed assembly of silicon tiles using fluid flow in a unstructured microfluidic chamber. Though most of these systems allow for some form of directed assembly, there are two limitations when applied to the development of macroscale programmable matter. The first is that the assembly occurs in 2D in a single plane. The second is that because they are of micro- or nanoscale dimensions, an inordinate number of these components would be required in order to create a macroscopic object.

Performing self-assembly on the macroscale introduces a new set of complications [11]. One fundamentally different aspect is that the assembly elements can be self-propelled as opposed to externally driven as is done on the microscale [12]. Systems of self-propelled units have been studied in the areas of reconfigurable [13] and modular [14] robotics. The suitability of these systems for programmable matter applications is constrained by the high power requirements for locomotion and limited mobility in three dimensions. Systems with externally propelled components have been used to implement self-replication in one [15] and two dimensions [16, 17]. Self-assembly of predefined shapes has also been demonstrated in two dimensions using passive, non-homogenous, magnetically-linking components [18]. Systems of homogenous and active components have been used demonstrate programmable assembly of regular shapes [19] and self-reconfiguration [20] using 12- and 6-cm scale components respectively. These systems employed an air table to agitate the

components; hence they are limited only to two dimensional structures. Currently there have been only limited attempts to create systems that operate in three dimensions. One successful approach is though self-disassembly [21]. In such a system the components start out in a 3D lattice and detach from each other to form the desired shape. While this simplifies the formation of an initial structure, for it to reconfigure into a general new structure, an assembly technique would be required to reform the original lattice. Another approach is to have the components agitated by a fluid in a three dimensional chamber as was demonstrated by White *et al.* [22]. The 10-cm scale of these components, though good for integrating functionality into the components, does not closely approach the resolution necessary for a programmable matter system.

In this work we investigate the use of cm-scale building blocks that are agitated in a stochastic flow pattern and assemble them in using local fluid forces using the general assembly scheme shown in Figure 2.1. Briefly, an assembly substrate provides the pumping force necessary for fluid agitation. As the fluid flows into an open valve on the substrate or building block, a fluidic sink is created. The flow of fluid into this sink will drag free floating blocks towards the associated docking site and align them. This alignment can be facilitated by a secondary force interaction between the docking site and the block; this interaction could be capillary [23], magnetic [19], or geometric [15]. We have previously analyzed the high-level dynamics of assembly in this type of system using a custom simulator with simplified fluidic forces[24].

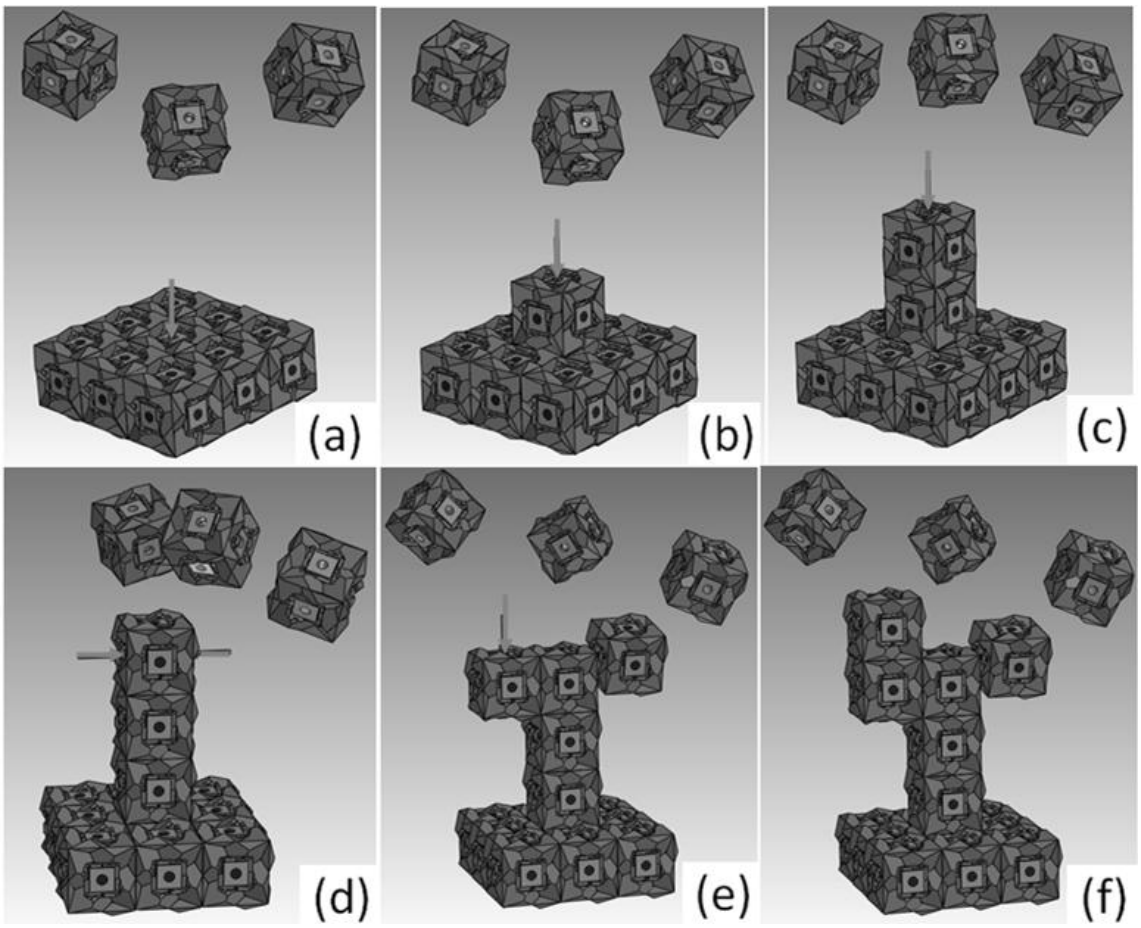

Figure 2.1 3D Fluidic Assembly: (a) Fluid forces attract blocks to the open sink. (b-d) Valves allow for the hydrodynamic affinity of blocks to be controlled to build the desired shape, (red indicates closed, green arrow indicated open). (e-f) A block that assembles in a misaligned fashion will not allow assembly to continue. Half of a wrench structure is completed, but assembly of the other half is stopped. A misaligned block can be rejected and assembly could be continued

In this paper, the crucial problem of component alignment during fluidic assembly is investigated using a combination of numerical simulations and experiments. Numerical simulations were conducted in order to study how blocks approach a sink in a stagnant flow to gain insight into dealing with the degrees of freedom in the system. The numerical results were used to design blocks for experiments in a

prototype assembly chamber. These experiments also allowed us to develop strategies for alignment.

2.3 Theoretical Analysis of Block Assembly

Two sets of simulations were conducted to study three dimensional hydrodynamically driven assembly. To begin a set of simulations were performed in order to generate a baseline for the motion of an unbiased block toward a fluid sink. The second set of simulations was conducted to test our hypothesis that if the degrees of freedom in the system could be limited alignment would be improved. One rotational degree of freedom could be eliminated by having blocks that align themselves with the gravity field due to an unbalanced mass distribution. Prior to discussing the results of these simulations, in this section details of the numerical method are provided.

In our simulation, the flow was assumed to be laminar and incompressible. The blocks were assumed to be neutrally buoyant and had no initial momentum. The motion of the fluid was described using the 3D, incompressible Navier-Stokes equations for a Newtonian fluid:

$$\frac{\partial \mathbf{u}}{\partial t} + \mathbf{u} \cdot \nabla \mathbf{u} = -\frac{1}{\rho} \nabla p + \nu \nabla^2 \mathbf{u} \qquad (2.1)$$

$$\nabla \cdot \mathbf{u} = 0 \qquad (2.2)$$

where **u** is the velocity of the fluid, p is the pressure, and ρ and v are the density and viscosity of the fluid respectively. The force, **F** and torque, $\mathbf{T_B}$ on the block are computed using the stress tensor, $\boldsymbol{\tau}$, such that:

$$\mathbf{F} = \int_A (\boldsymbol{\tau} \cdot \mathbf{n}) \mathrm{dA} \qquad (2.3)$$

$$\mathbf{T_B} = \int_A (\mathbf{r} \times (\boldsymbol{\tau} \cdot \mathbf{n})) \mathrm{dA} \qquad (2.4)$$

where A is the surface of the body, and **n** is the surface normal. $\mathbf{T_B}$ refers to the torque with respect to the body co-ordinates. The simulations were performed using the CFD simulation package, FLOW-3D. An explicit method was used to conduct the simulations: fluid and block motions at each time step were calculated using the force and velocity data from the previous time step; similar to the approach taken by Krishnan *et al.* [10].

2.3.1 Characterization of Block Motion toward Docking Site as a Function of Initial Conditions

The first set of simulations was conducted to determine the range of initial approach conditions that lead to proper alignment of blocks at a docking site. The domain was constructed as shown in Figure 2.2 (a). The initial position of the block was varied by setting two angles: The initial polar angle θ between the block and a normal to the sink, and the block's initial clockwise angle of rotation φ. This setup represents an attempt to model the fact that blocks can approach the sink from any angle and have any orientation with respect to their center of mass. The blocks were

started 2 cm away from the sink and were 1 cm on each side. In total 16 simulations were performed, testing the combinations of 4 values of θ (0°, 30°, 60°, 90°) and 4 values of φ (0°, 15°, 30°, 45°). The results are shown in Table 2.1. As expected, the case of θ = 0°, φ = 0° lined up perfectly with the docking site (Figure 2.2b). By contrast, the cases of θ = 90° did not closely approach the docking site since the sink force is weakest parallel to the docking site (the center of the block was more than 6 mm away from the sink, Figure 2.2b). In the rest of the cases the block approached the docking site with the corner at an angle, due to the action of hydrodynamic torque (Figure 2.2d). This type of approach makes it very difficult for any secondary interaction (e.g. magnetic, geometric or capillary) to align the blocks, since the block is misaligned in all three planes.

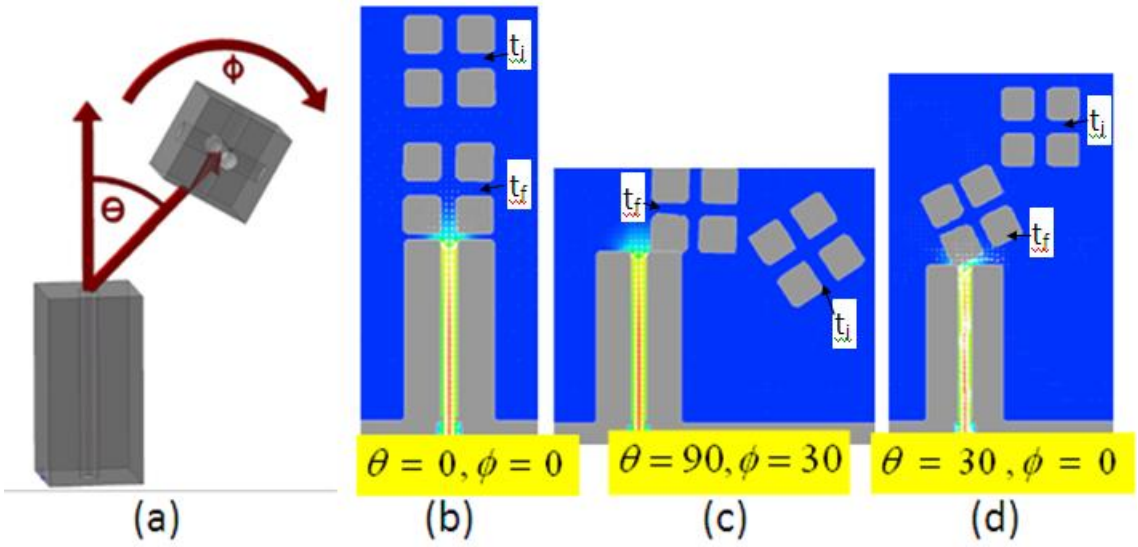

Figure 2.2 Characterization of Block Motion: (a) The approach angle, θ, and the angular position of the block with respect to its center of mass, φ, were varied to over 16 simulation cases. The center-to-center distance between the cube and the sink is a constant 2 cm. (b) Illustration of the results of two cases, showing the initial and final position of the block with respect to the pedestal.

θ	$\varphi = 0°$	$\varphi = 15°$	$\varphi = 30°$	$\varphi = 45°$
0°	Aligned	Corner On	Corner On	Corner On
30°	Corner On	Corner On	Corner On	Corner On
60°	Corner On	Corner On	Corner On	Corner On
90°	6mm+	6mm+	6mm+	6mm+

Table 2.1: Results for Uniform Block Simulations

2.3.2 Effect of Limiting the Degrees of Freedom on Block Alignment

Limiting the degrees of freedom in the motion of the blocks is one method by which the *Corner On* docking observed above could be reduced. This can be done by giving the block an unbalanced mass distribution such that when it is perturbed it experiences a restoring torque to align itself with the gravity field. As a first order approximation, in our simulations we modeled this by constraining the motion of the moving block so that it could not rotate about the φ axis. This assumption is valid so long as restoring torque is much larger than the hydrodynamic torque. The motion of these blocks was simulated for the representative cases shown in Figure 2.3 [24]. These four cases are: a block was attracted to a wall with a sink, a pedestal with a sink open at the top, a pedestal with a sink open at the side, and a corner structure with two sinks open. In each case, the initial polar angle θ was varied over a range of values and the blocks were initialized 2 cm away from the sink as in the uniform block simulations.

Since these blocks were not allowed to rotate to point an edge at the sink, they could approach the sink and still be in a position to dock. To characterize how well a block docked we use the horizontal component of the final center-to-center distance between the block and the sink, *x*. This is plotted for the four cases in Figure 2.4 for the cases described above. The trends observed for each case are similar, even though the geometry is different. More specifically as θ increases, the block's final position is farther away from the sink increases as well. For the majority of the cases the block comes within 5 mm (50% if normalized by block size) of sink, meaning that it is halfway aligned. The trend is that for each case there is a ±20° range in θ that yields a fairly high probability of docking. Beyond this 20° cone performance is poor.

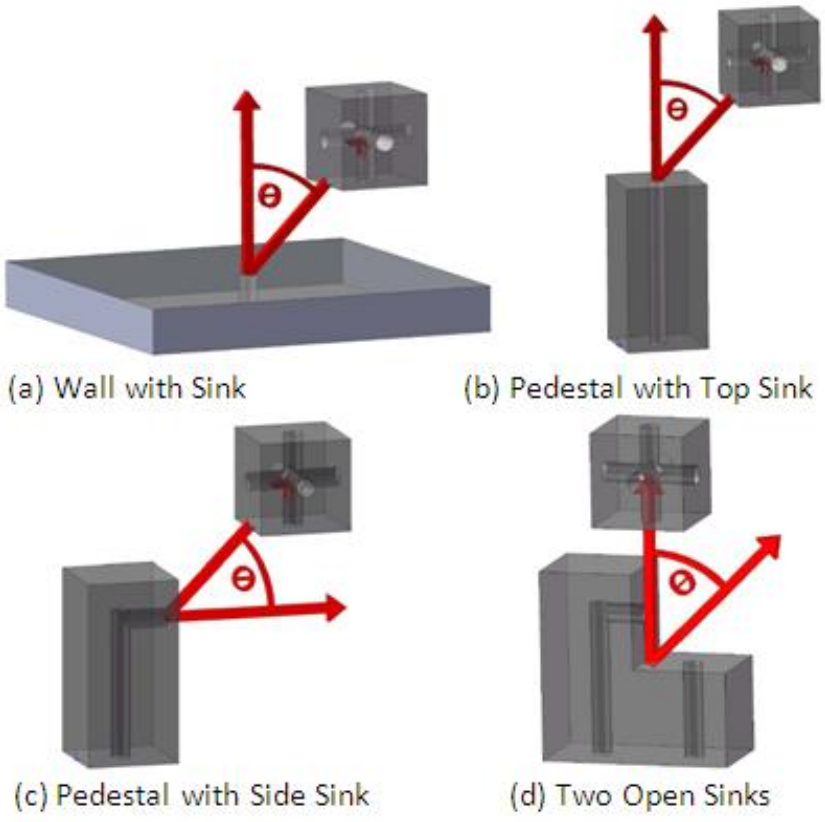

Figure 2.3: Basic Assembly Cases with the variable θ indicated**:** These 4 cases represent the possible docking scenarios during the assembly of a large structure[24].

To conclude, the simulations have demonstrated that: a) the hydrodynamic torque on uniform density blocks will bring them to the docking site in a misaligned corner first position; b) reducing the rotational degrees of freedom can improve alignment; c) only a relatively small percentage of blocks will approach close enough to the docking site to allow a secondary interaction to align the block..

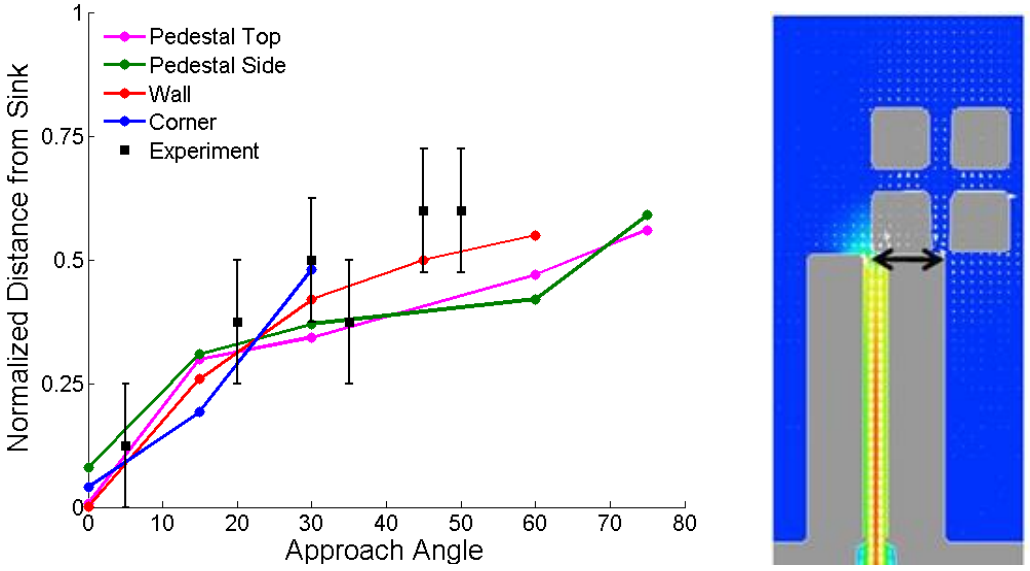

Figure 2.4: Simulation Results and Experimental Validation. The final distance (measured as illustrated in the inset) between the center of block and sink as a function of the approach angle, θ.

2.4 Experimental Characterization of Block Docking

We performed three sets of experiments to develop and characterize our docking method. The first set of experiments centered on physically implementing our idea for limiting the degrees of freedom of the blocks by giving them an unbalanced mass distribution. In the second set of experiments, we tested the effect of block topography on assembly alignment. In the third set, we developed a protocol for achieving aligned

assembly. An assembly chamber was constructed to carry out these experiments and can be seen in Figure 2.5.

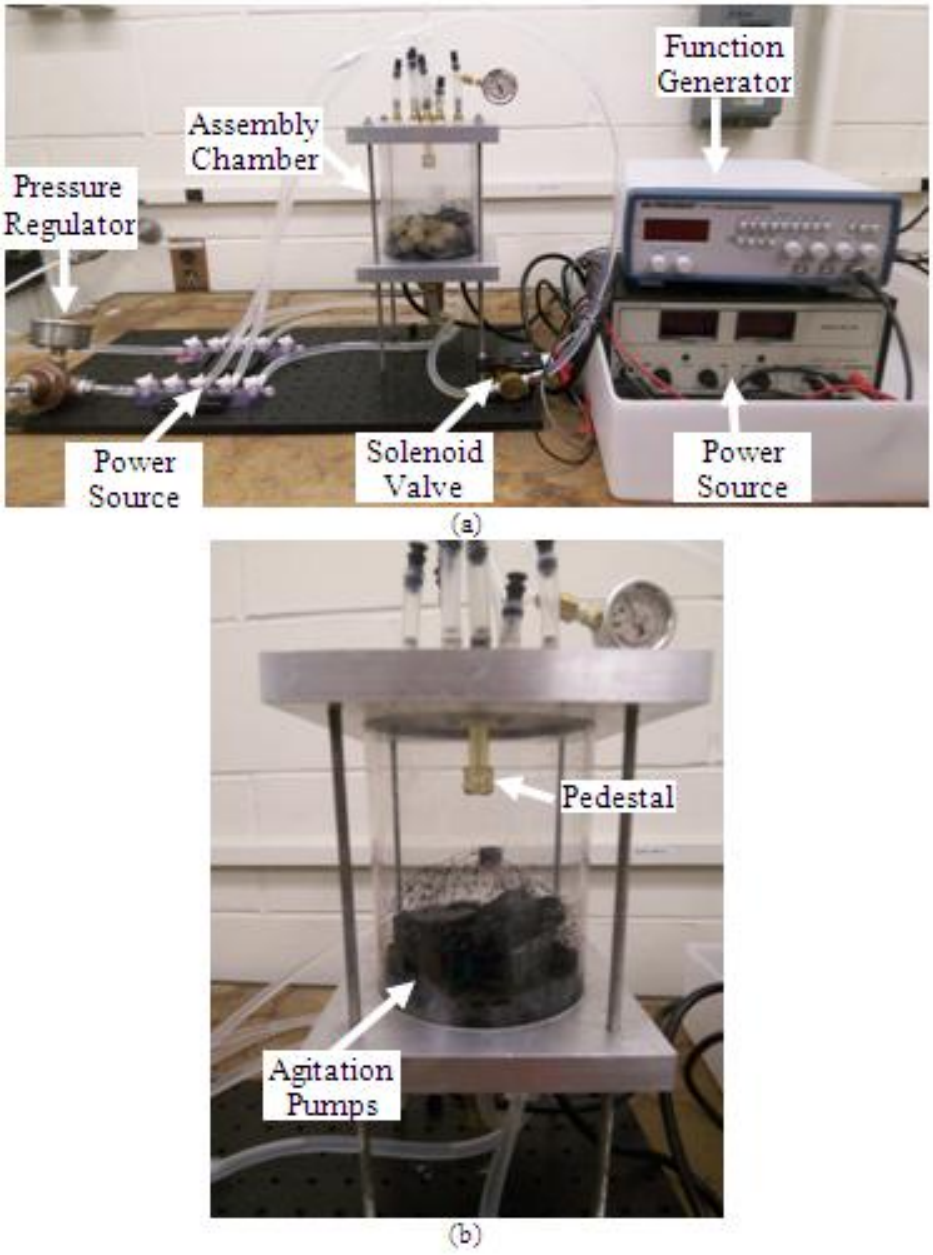

Figure 2.5: Assembly chamber for experiments. (a) Overall Setup. (b) Close up of chamber. The pressure in the chamber is controlled by an inflow pressure regulator. The assembly chamber has inlets and outlets that are controlled by several valve manifolds. One of the outlets goes through the pedestal docking site. A solenoid valve is used to pulse the flow through the pedestal and is controlled by the function generator and power source (used in the third set of experiments).

In this apparatus, water is pumped into the chamber and is allowed to exit through a series of outlets and through the pedestal (which can be seen in the inset) forming a fluid sink at the desired location for the blocks to be attracted. The pressure in the chamber controls the strength of the sink and is set by the inlet pressure regulator. The blocks are agitated in the chamber by a combination of a circulatory flow, which is created by two small circulation pumps, and jet flows from inlets at the top of the chamber. The jets flows were used to push the blocks down since the blocks are buoyant in water. Additionally, a solenoid valve that can be used to create pulsations in the outflow was used in the third set of experiments.

2.4.1 Experimental Validation of Simulations

Operation of the assembly chamber is illustrated in Figure 2.6, which shows time lapse images of a single cube docking and then being rejected from the pedestal. Blocks circulate throughout the chamber and attach to the sink when they approach the sink, as in Figure 2.6 (a)-(c). Once a block is attached, it can be aligned (the steps for this are described below in Section 2.4.3), and then rejected to conduct another trial. This cube rejection also demonstrates the system's error correction method and reconfigurability. A video of this operation is presented in Online Resource 1.

For successful assembly, blocks have to be aligned to the docking site in three planes. The results of the simulations indicated that alignment in one plane can be generated by making the assembling blocks behave in such a way that one face preferentially orients itself as the top. In these experiments the blocks were

manufactured using a 3D printer (rapid prototyping machine) that allowed for a hollow space to be left next to one face of a block, as seen in Figure 2.7(a). This resulted in the buoyancy driven restoring torque on the blocks analogous to that described above in the simulations. The blocks used in these experiments were 1cm on a side. The docking behavior of these blocks was characterized by repeatedly attracting blocks to the pedestal and then releasing them, as in Figure 2.6 (a)-(c). Their motion was recorded by a camera. 25 blocks were used to populate the chamber in this experiment.

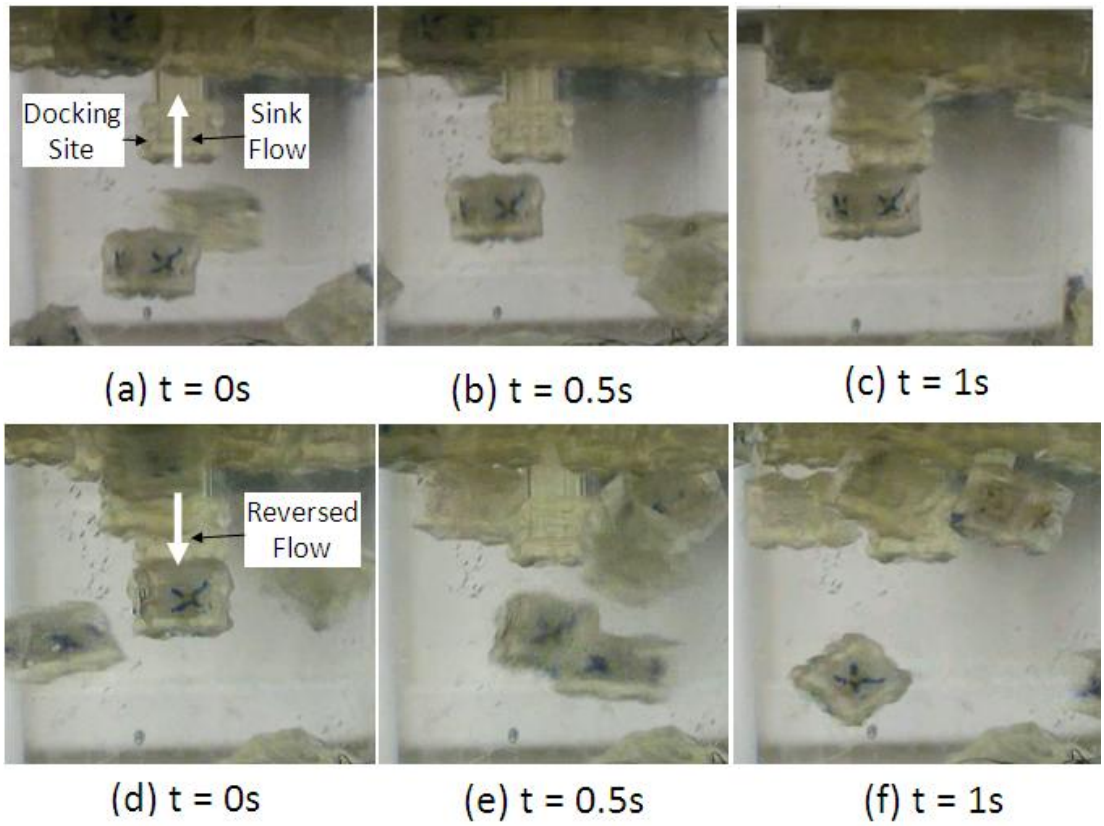

Figure 2.6: Time lapse images of a block docking and undocking with the pedestal. (a)-(c) A block from the general flow docks with the pedestal in a misaligned fashion. It is aligned by using the strategy described in section 3.3. (c)-(d) The block is released from the pedestal by reversing the flow through the sink. This method releases blocks in every case, independent of whether the block aligns or misaligns.

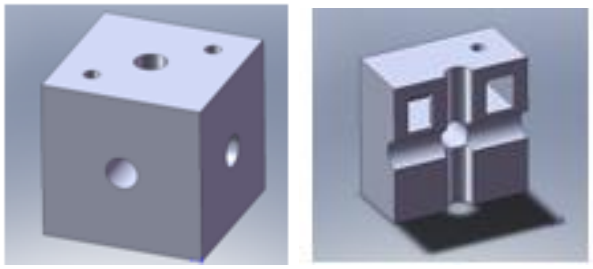

(a)

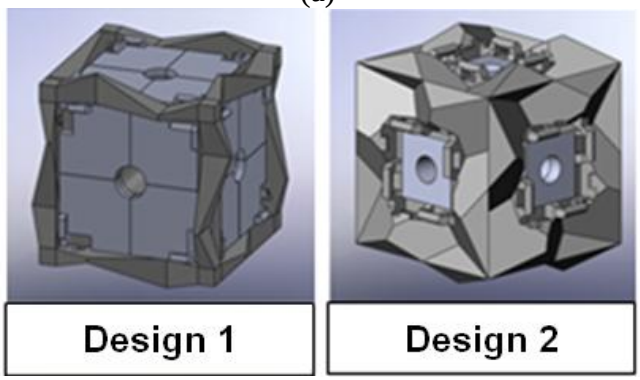

(b)

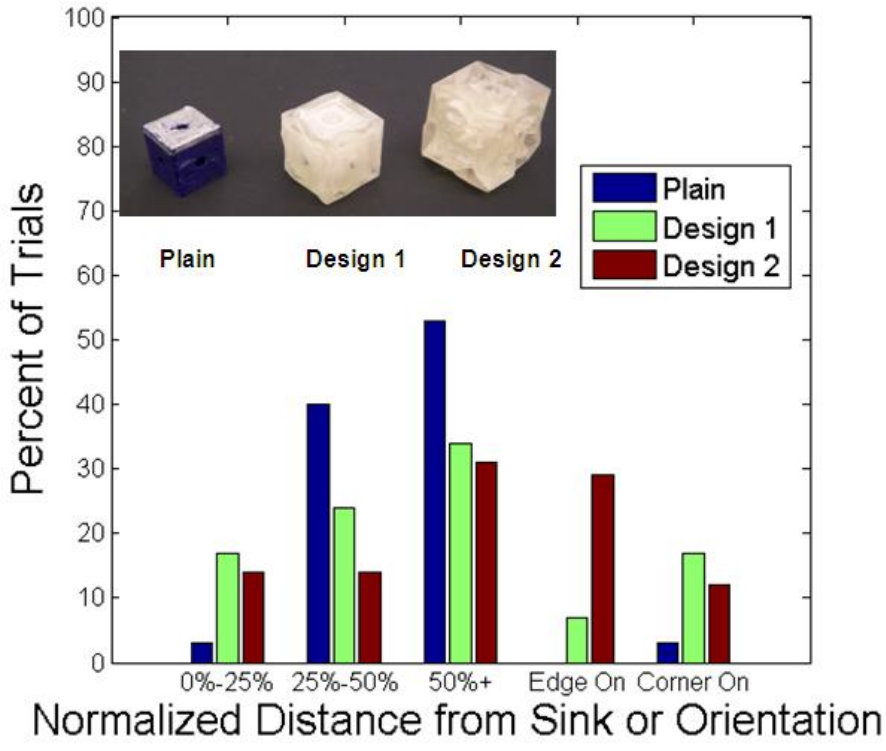

(c)

Figure 2.7: Effect of Block Topography. (a) CAD model of 3D printed cubes with hollow space for an unbalanced mass distribution (b) CAD models of two block designs that were tested. (c) Histograms of final positions of blocks in for trials with the 3 block designs shown.

The results of this experiment are presented in Figure 2.4 (a) and 2.7 (c). In Figure 2.4(a), the final position of the block with respect to the pedestal is plotted as a function of approach angle for the simulations and the experiment. A similar trend is observed in both cases with smaller angles yielding closer final positions. The experimental results indicate that at high approach angles the final position of the block is worse than predicted by the simulations. This could be due to the fact that the simulations did not account for the initial translational and rotational momentum of the blocks that is generated by the agitating flow. A histogram of the final positions of the docking block is presented in Figure 2.7(c). Only in a small percentage of trials (3%), did block ended up in the Corner On position: misaligned with its corner in the sink. In 43% of trials the final position of the block was within half the length of the block's side (5 mm). The high percentage of blocks that were outside of this 50% zone is the result of the fact that a majority of the blocks approached the pedestal with high approach angles.

2.4.2 Effect of Block Topography

Several block geometries were tested in order to encourage alignment in the two planes perpendicular to the plane of the sink opening. Two representative designs are analyzed here, which we call *Design 1* and *Design 2* (Figure 2.7 b). When two such blocks were pressed together they self-aligned due to geometric interactions. Additionally, these blocks have latches to stay attached once they are assembled and they are slightly larger than the plain cubes from the previous experiments, 1.2 cm for *Design 1* and 1.5 cm for *Design 2*, due to the limitations of the 3D printer in resolving

the added features. We repeated the experiment described in the previous section with these new blocks designs. In these cases, 15-20 blocks were used to populate the chamber and were repeatedly attracted to and released to the pedestal. Adding more blocks would create jamming between them and slow the rate at which trials could be conducted.

The distributions of the final positions of the blocks in each of the experiments are presented in Figure 2.7(c). The number of blocks that ended very close to the sink (within 25% of the block length) increased for the new designs. An increase in size and weight contributed to this fact since now more blocks approached the pedestal from below and with correspondingly shallower approach angles. Another result is that adding topography to the cube surfaces allowed them to end up in a new final position, which was designated *Edge On*, due to the extra geometric interactions between the block and pedestal surfaces. In this position one edge of the block covers the sink hole in the pedestal, as opposed to *Corner On* where one of the corners covers the sink hole. As the geometrical complexity on the block design increased, so did the percentage of trials that reached the *Edge On* position. Though these new block designs also had an unbalanced mass distribution, an increase in the instances of the *Corner On* position was observed, but was kept to below 20%. Most importantly, adding topography to the blocks did not generate aligned assembly.

2.4.3 Effect of Flow Pulsation

The experiments described in section 2.4.2 showed that adding geometric interaction is not enough to generate aligned assembly. A more successful strategy

was achieved by adding a solenoid valve to the outflow from the pedestal. This allowed for the flow to be pulsed after a block initially docks in a misaligned manner. The best results were yielded by a 3 Hz pulsation rate, since at this frequency enough block motion was generated to allow the geometric interactions to align the block. At lower frequencies the block could be released to the outer flow, and at higher frequencies the amplitude of the blocks oscillation was too low to allow it to change positions. Experiments were conducted with *Design 1* and *Design 2* blocks. In experiments with the *Design 1,* alignment was never observed over the course of more than 50 trials. However, the *Design 2* blocks were more successful.

During experimental trials with the *Design 2* blocks and flow pulsation, a 54% rate of aligned docking was observed. The average time for a block to get attracted to the docking site was 30s, and the average additional time required for a successful alignment was 24s. The success with which the flow pulsation was able to align the block depended on the initial (misaligned) position that a block took relative to the pedestal (Figure 2.8). We observed that the closer the blocks came to the sink initially, the more likely they were to fully align (as expected). Surprisingly, more than half the blocks that misaligned in the *Corner On* position were righted and fully aligned. However, there were trials where blocks reached a position from which it was impossible to achieve alignment (*i.e.* the previously discussed *Edge On* position).

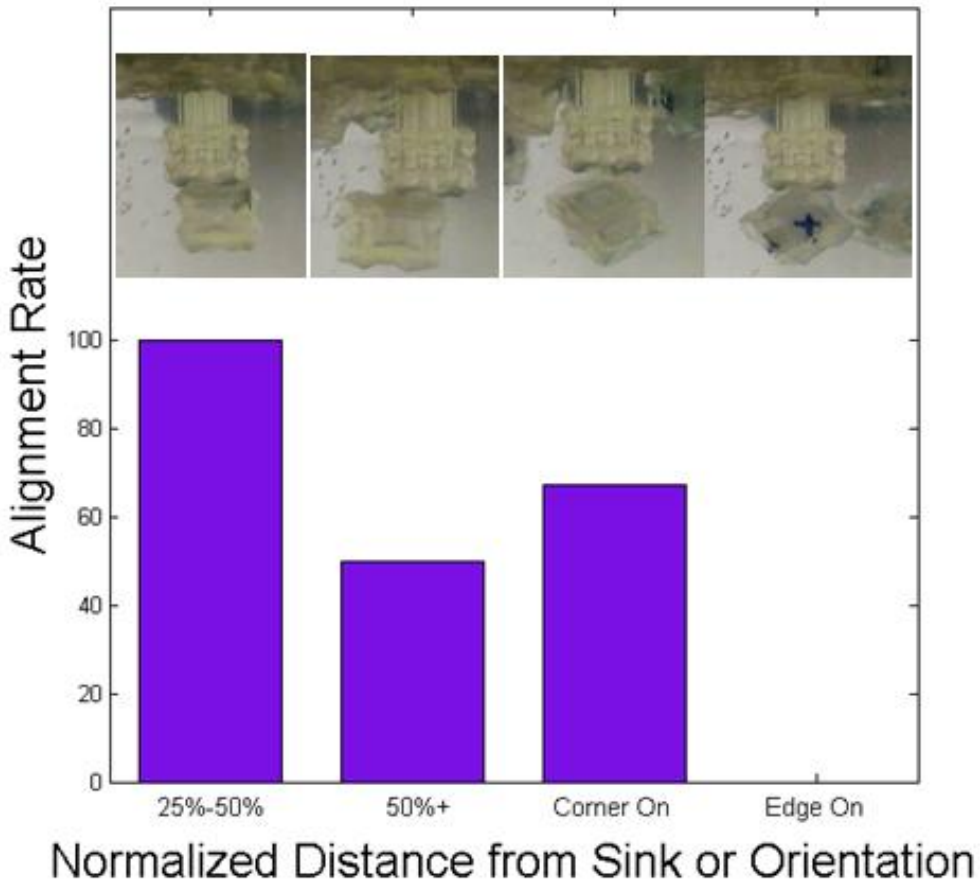

Figure 2.8: Initial Position of Blocks vs. Alignment. Pulsing the sink flow caused the alignment of majority of blocks whose initial position was not close to the sink or that were in a misaligned orientation in all three planes (corner sucked into sink). In some trials, blocks had their edge sucked into sink and could not be aligned.

2.5 Discussion and conclusions

3D fluidic assembly is an approach that can be used to implement a programmable matter system. In this work we concentrated on understanding the phenomenon at one docking site and demonstrated the ability to assemble a single free floating block using a three dimensional flow field. Achieving proper alignment is necessary for adding further blocks to the structure and creating larger useful structures. Numerical simulations showed that this cannot be done using fluid motion alone. It was shown

that the sink flow can be used to bring blocks to the docking site, but the blocks could be misaligned in all three planes. Blocks with an unbalanced mass distribution were shown to counteract misalignment in the vertical plane. Misalignment in the other two planes was dealt with using two effects. First, blocks were designed to interact with each other through complex geometric interactions. Secondly, a pulsating sink flow facilitated final alignment after a block had been attracted to a docking site. The combination of these methods allowed for the blocks to be successfully docked in 54% of trials. Our system has demonstrated the ability of 3D fluidic assembly to operate on the cm-scale. This is useful for the assembly of macroscale objects with a reasonable resolution. The next steps will be to demonstrate the assembly, reconfiguration, and disassembly of multi-block structures by valving the channels in the blocks..

2.6 Acknowledgements

We thank Mekala Krishnan, Jonas Neubert and Abraham Cantwell for useful discussions regarding fluidic assembly and cube design. This work is supported by the Defense Advanced Research Projects Agency Defense Sciences Office under the "Programmable Matter" program.

REFERENCES

1. Liddle, J.A., Y. Cui, and P. Alivisatos, *Lithographically directed self-assembly of nanostructures.* Journal of Vacuum Science & Technology B, 2004. **22**(6): p. 3409-3414.
2. Morris, C.J. and B.A. Parviz, *Self-assembly and characterization of Marangoni microfluidic actuators.* Journal of Micromechanics and Microengineering, 2006. **16**(5): p. 972-980.
3. Srinivasan, U., D. Liepmann, and R.T. Howe, *Microstructure to substrate self-assembly using capillary forces.* Journal of Microelectromechanical Systems, 2001. **10**(1): p. 17-24.
4. Avital, A. and E. Zussman, *Fluidic assembly of optical components.* IEEE Transactions on Advanced Packaging, 2006. **29**(4): p. 719-724.
5. Sharma, R., *Thermally controlled fluidic self-assembly.* Langmuir, 2007. **23**(12): p. 6843-6849.
6. Chung, J.H., et al., *Programmable reconfigurable self-assembly: Parallel heterogeneous integration of chip-scale components on planar and nonplanar surfaces.* Journal of Microelectromechanical Systems, 2006. **15**(3): p. 457-464.
7. Mastrangeli, M., et al., *Self-assembly from milli-to nanoscales: methods and applications.* Journal of Micromechanics and Microengineering, 2009. **19**(8).
8. Chung, S.E., et al., *Guided and fluidic self-assembly of microstructures using railed microfluidic channels.* Nature Materials, 2008. **7**(7): p. 581-587.
9. Tolley, M.T., et al., *Dynamically programmable fluidic assembly.* Applied Physics Letters, 2008. **93**(25).

10. Krishnan, M., et al., *Increased robustness for fluidic self-assembly*. Physics of Fluids, 2008. **20**(7).

11. Whitesides, G.M. and M. Boncheva, *Beyond molecules: Self-assembly of mesoscopic and macroscopic components.* Proceedings of the National Academy of Sciences of the United States of America, 2002. **99**(8): p. 4769-4774.

12. Gross, R. and M. Dorigo, *Self-assembly at the macroscopic scale.* Proceedings of the IEEE, 2008. **96**(9): p. 1490-1508.

13. Castano, A., A. Behar, and P.M. Will, *The Conro modules for reconfigurable robots.* IEEE-ASME Transactions on Mechatronics, 2002. **7**(4): p. 403-409.

14. Dorigo, M., et al., *Evolving self-organizing behaviors for a swarm-bot.* Autonomous Robots, 2004. **17**(2-3): p. 223-245.

15. Penrose, L.S. and R. Penrose, *Self-Reproducing Analogue.* Nature, 1957. **179**(4571): p. 1183-1183.

16. Griffith, S., D. Goldwater, and J.M. Jacobson, *Robotics - Self-replication from random parts.* Nature, 2005. **437**(7059): p. 636-636.

17. Breivik, J., *Self-organization of template-replicating polymers and the spontaneous rise of genetic informations.* Entropy, 2001. **3**(4): p. 273-299.

18. Bhalla, N. and P.J. Bentley. *Working towards self-assembling robots at all scales*. in *Proc. 3rd Int. Conf. Auton. Robots Agents*. 2006. Palmerson North, New Zealand.

19. Klavins, E., *Programmable Self-assembly.* IEEE Control Systems Magazine, 2007. **27**(4): p. 43-56.

20. White, P.J., K. Kopanski, and H. Lipson. *Stochastic self-reconfigurable cellular robotics*. in *Proc. 2004 IEEE Int. Conf. Robot. Autom.* 2004. Los Alomitos, CA.

21. Gilpin, K., et al., *Miche: Modular shape formation by self-disassembly.* International Journal of Robotics Research, 2008. **27**(3-4): p. 345-372.

22. White, P., et al. *Three Dimensional Stochastic Reconfiguration of Modular Robots*. in *Proceedings of Robotics Science and Systems*. 2005. MIT.

23. Gracias, D.H., et al., *Forming electrical networks in three dimensions by self-assembly.* Science, 2000. **289**(5482): p. 1170-1172.

24. Tolley, M.T., et al., *Stochastic Modular Robotic Systems: A Study of Fluidic Assembly Strategies.* Robotics, IEEE Transactions on, 2010. **26**(3): p. 518-530.

CHAPTER 3

IN SITU HOLLOW FIBER MEMBRANE FACILITATED CO_2 DELIVERY TO A CYANOBACTERIUM FOR ENHANCED PRODUCTIVITY

3.1 Abstract

Recently, cyanobacteria have been metabolically engineered to secrete valuable biofuel precursors eliminating the requirement to harvest and post-process algal biomass. However, development of new photobioreactors (PBRs) that can efficiently deliver light and address the mass transport challenges associated with maintaining high cyanobacteria productivity has been lagging. Hollow fiber membranes (HFMs) are a method for bubble-less gas exchange that has been shown to be effective at enhancing mass transfer. Previous applications of HFM technology to PBRs have been limited to exploring its ability to enhance CO_2 delivery to the bulk liquid volume. To investigate potential strategies for novel PBR design configurations, we examined the growth pattern of *Synechococcus elongatus* around individual hollow fiber membranes to determine the optimal spacing and conditions for maximizing photosynthetic activity. We have shown that a single fiber enabling passive transport from/to the atmosphere can provide enough gas exchange to increase biomass accumulation by > 2.5 times with respect to a non-fiber control. This increased growth was found to decay in the radial direction with the enhanced growth area spanning between 1.2 mm and 1.7 mm depending on the initial inoculation concentration.

*Reprinted by permission of the Royal Society of Chemistry with permission from Michael Kalontarov, Devin F. R. Doud, Erica E. Jung, Largus T. Angenent and David Erickson "*In situ* hollow fiber membrane facilitated CO_2 delivery to a cyanobacterium for enhanced productivity". *RSC Advances*, 2013. **3**: p. 13203-13209., http://dx.doi.org/ 10.1039/C3RA40454D © RSC

3.2 Introduction

Biofuels have been proposed as a solution to problems arising from fossil fuel usage such as CO_2 emissions, climate change, and energy security [1]. These fuels are derived from photoautotrophic organisms that fix inorganic carbon (CO_2) into useful biomolecules, and therefore these biofuels have the potential to be carbon neutral [2]. The most common organisms used for this purpose are plant crops. However, their usage has come under widespread scrutiny for two reasons: i) inefficiencies associated with crop-based biofuel production[3]; and ii) competition for land use with traditional agriculture, thereby putting pressure on the food supply, encouraging deforestation, and increasing carbon emissions [4]. The use of photosynthetic microorganisms, such as cyanobacteria and micro-algae address both of these problems with their high CO_2 fixation efficiencies, fast growth rates, and potential to utilize waste-water or industrial gas wastes as nutrient sources [2]. Currently, the most developed method for harnessing the energy producing capabilities of these organisms is to convert their stored lipids into biodiesel [5].

Two major limitations for the widespread adoption of algal biodiesel are inefficiencies in lipid extraction and biomass cultivation [6]. Technologies that allow for direct extraction of soluble biofuels, or biofuel precursors, from a photobioreactor (PBR) could mitigate the difficulties that arise during the extraction/dewatering/refinement processes inherent to biodiesel production. One such advance comes with the development of engineered strains of cyanobacteria that have the ability to directly secrete fuels such as hydrogen [7, 8], ethanol [9, 10], isobutyraldehyde [11] and other high value products [12]. Specifically,

isobutyraldehyde production in an engineered strain of *Synechococcus elongatus* has been performed at area-wise efficiencies comparable to or greater than bioethanol and biodiesel [13]. In parallel with these advances, limitations in biomass cultivation could be addressed by improving the state-of-the-art in bioreactor engineering.

Algal biomass is most commonly cultivated in open raceway ponds and tubular PBRs [14]. Open pond reactors offer a low cost and low energy approach, but also low productivity, while tubular PBRs offer much higher productivity at the cost of high energy and capital input [15]. To improve biomass cultivation, the fundamental limitations that need to addressed by new PBR designs are efficient delivery of light and inorganic carbon to the bacteria, and the removal of dissolved oxygen and other products including soluble fuels [16]. These limitations can be addressed by creating ultra-compact PBRs that attempt to enhance transport of both light and nutrients, and facilitate the extraction of products at the bacterial scale to increase volumetric and footprint efficiencies. We have recently demonstrated an architecture by which light can be delivered to a bacterial layer in a compact manner [17]. The work presented here attempts to compliment this technology by addressing limitations in inorganic carbon transport.

The typical method for inorganic carbon delivery used in open ponds and tubular PBR designs is the aeration of growth media by exposure to the atmosphere or bubbling [18]. Though this has been shown to be effective, disadvantages include inefficiencies with incomplete CO_2 utilization or losses to the atmosphere (depending on whether an open or closed system approach is used), and unequal transport throughout the reactor [19]. Hollow fiber membranes (HFMs) are a technology that

allow for bubble-less gas exchange and have been used in a wide variety of engineering and bio-engineering applications including the treatment of wastewater [20] and landfills [21]. HFMs are attractive for photobioreactor engineering since they allow for both CO_2 delivery and O_2 removal as a function of their partial pressures across the membrane [22, 23]. In addition, another potential advantage is the ability to extract soluble products using compatible HFMs. In the last decade, researchers have applied HFM technology to photobioreactors by incorporating HFM modules and have demonstrated improved CO_2 sequestration and biomass growth rate with a range of cyanobacteria and microalgae [23-26].

Several parameters have to be optimized to directly apply HFMs in compact reactor designs. Chief among them is the maximum spacing that can separate the fibers while still maintaining an adequate gas exchange rate to support photosynthetic growth and fuel production. Having fibers spaced farther apart than optimum would result in zones of low CO_2 concentration and limited productivity. On the other hand, a closer spacing of the fibers would result in an inefficient use of reactor volume since more of the reactor space would be used up by the fibers unnecessarily. In this study, we characterized the growth of *S. elongatus* in CO_2 limited conditions where a single HFM fiber served as the only CO_2 source. Changes in the bacterial distribution as a function of time for several initial bacteria concentrations were characterized and compared to controls.

3.3 Materials and Methods

The experimental setup consisted of sealed miniature reactors measuring 40 mm × 16 mm × 6 mm. A single HFM fiber (model no. MHF304KM purchased from the Mitsubishi Rayon Co., Ltd.) centered on the bottom of the reactors along the primary axis (Figure 3.1), was exposed to the atmosphere on both sides and used for passive gas delivery throughout the course of the experiments. The MHF304KM is a multilayered composite hollow fiber membrane, composed of a non-porous ultra-thin membrane sandwiched between two porous membranes. The reactors were constructed with a microscope glass slide foundation and a PDMS chamber positioned on top. The HFM fiber was aligned in between the center of the PDMS cover and glass slide. A glass cover-slip was fixed atop the PDMS ceiling to reduce gas diffusion into the reactor. All walls and joints were sealed with KwikWeld Epoxy (J-B Weld Company) to make the reactors as gas tight as possible. Reactors without the HFM fiber served as controls for CO_2 delivery. *Synechococcus elongatus* SA665, which has been engineered to produce isobutyraldehyde from CO_2, was obtained from the Liao lab at UCLA [11]. The reactors were inoculated with *S. elongatus* SA665 resuspended in modified BG-11 media with no carbon and the addition of a 50 mM phosphate buffer (pH 7.0) [11]. The media was made carbon free by eliminating bicarbonate and by sparging with N_2 for 30 min in an anaerobic serum bottle prior to re-suspension and inoculation of *S. elongatus*. Bacteria grown in this media are CO_2 limited and only experience growth at sources of CO_2 flux, only two of which exist in our reactors: the fiber and the reactor walls. As will be illustrated in Figure 3.3(b) and

Figure 3.4(a) the flux through the walls is very limited so the bacteria do not experience a continuous growth phase in the non-fiber reactors.

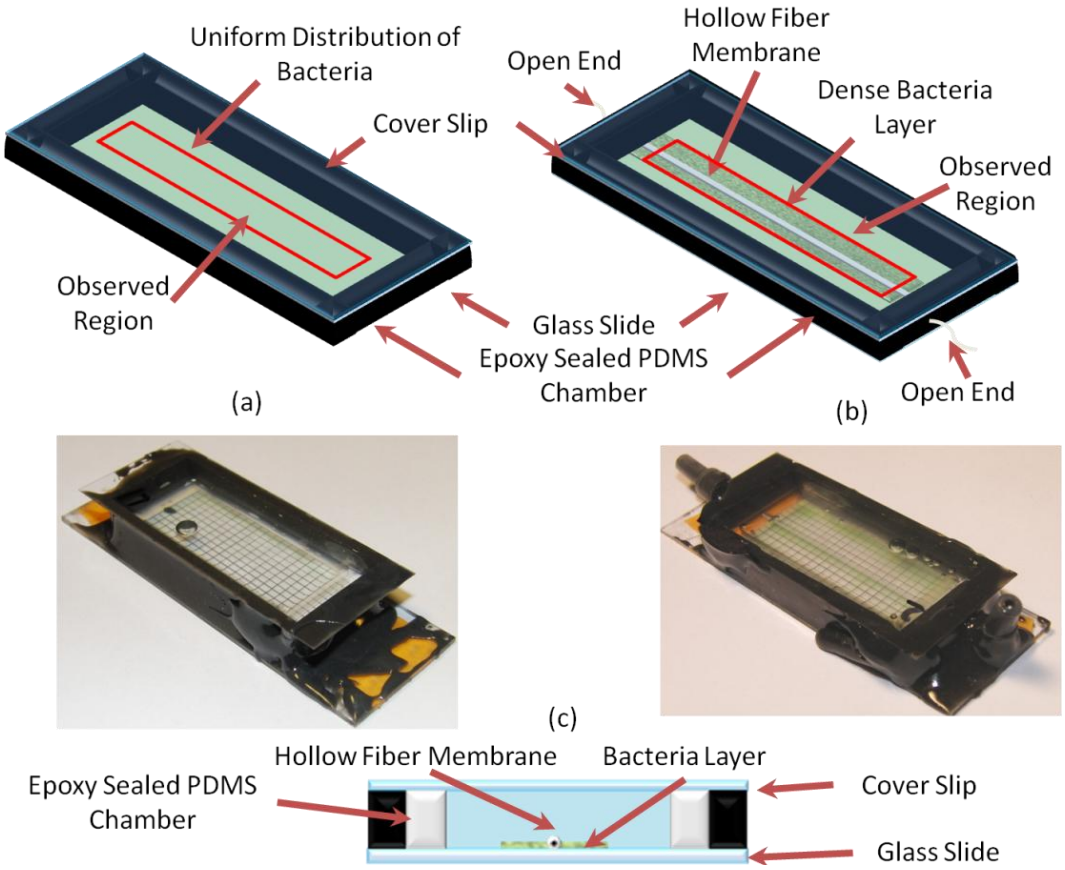

Figure 3.1 Experimental and control reactors: Schematic representation of the reactors, with the observed region indicated and photographs after 5 days of growth. (a) Fiber-less control reactors. (b) Reactors with a fiber showing a dense layer forming next to the fiber. (c) Z-axis cross-section of the reactor.

After inoculation was completed the reactors were sealed, shaken for a uniform initial distribution, and placed into either light or dark conditions. Two fluorescent light strips (American Fluorescent Plug-in Light Strip), which were positioned above the reactors, provided uniform illumination. Photon flux density in the plane of the reactors was measured to be 75 $\mu E\ s^{-1}\ m^{-2}$. The reactors were operated at laboratory room temperature measured to be 25°C. Growth in the reactors was imaged via

chlorophyll fluorescence under an upright fluorescence microscope (Olympus BX51) using a 5x objective and a CCD camera (Sony XCD-X710). Excitation light was provided by a mercury lamp and a Chroma Cy5 filter cube was used to filter the excitation (620 nm, 60 nm bandwidth) and emission (720 nm, 75 nm bandwidth) light. High contrast images of the bacteria in reactor were used to characterize the bacterial distribution along the length of the fiber. The images had a pixel resolution of ~1.8 μm, and this allowed for adequate imaging the bacteria, which have average dimensions of 3.5 ± 1.6μm in length and 1.7 ± 0.2μm in width, while also allowing us to observe a large extent of the reactor. Figure 3.2 depicts the bacteria size distribution. Bacteria whose size is much smaller than the average would lead to partially covered pixels, and this will introduce some error in our image processing.

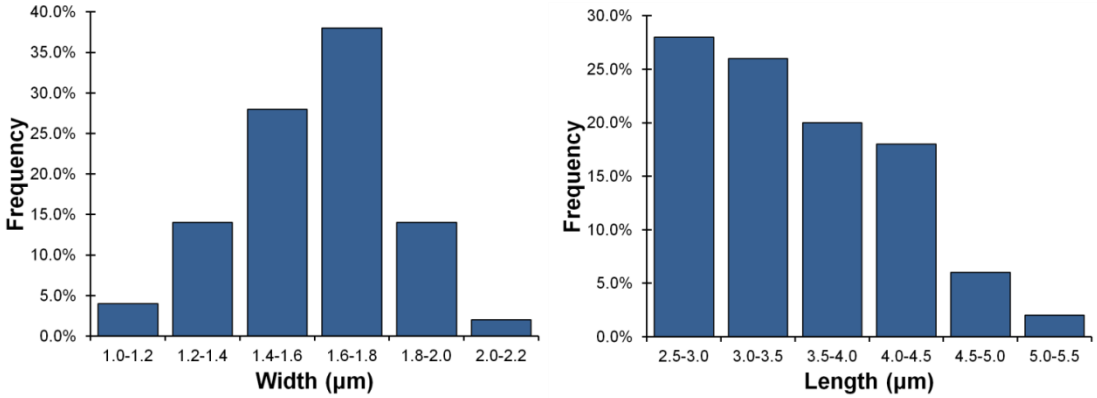

Figure 3.2 S. Elongatus size distribution (n=50).

Surface density, which represents the percentage of the two-dimensional reactor area that is covered by bacteria, was used to quantify bacterial growth. This quantity was calculated locally by first dividing the obtained fluorescence images into 128-by-128 pixel squares, corresponding to a physical area of approximately 235-by-235 μm. In each square we identified the pixels containing bacteria and divided by the total

number of pixels in the square to obtain the local surface density expressed as a percentage. The fluorescence intensity of each pixel was used only in a binary fashion in our analysis to identify whether bacteria are present. This allowed us to map out the area next to the fiber and develop a grid description of the bacterial distribution. If a pixel is covered by more than one bacteria, that pixel is only counted once in the surface density calculation because surface density is inherently a 2D quantity. The area of interest that was observed was a rectangle of approximately 2.8 mm-by-26 mm that was centered on the fiber and corresponded to a grid of 12 by 112 squares for which the local surface density was calculated. The width of this rectangle had been determined to be the range over which to monitor growth during preliminary experiments. The observed rectangle was offset from all of the walls of the reactor by a minimum of 5 mm. Preliminary experiments were done to confirm that this offset was long enough to prevent edge effects from interfering with the observed region. By averaging the local surface density over the area of interest, we obtained the total surface density.

We conducted trials with a range of reactor inoculation values corresponding to initial surface densities of 0.35%, 2.5%, and 6.0% coverage. This allowed us to characterize effects of CO_2 delivery from the fiber on growth for over an order of magnitude variation in the starting concentration, specifically to see if growth became limited at higher densities. Each trial consisted of 9 reactors placed in the dark, and 9 placed in the light. In each case, 6 reactors had fibers and 3 did not. The reactors placed in the dark served as the controls for carryover growth from the pre-culture and settling out patterns of bacteria as opposed to growth. The reactors without fibers

served as controls for determining the baseline amount of growth occurring without the presence of a HFM. All reactors were imaged daily using a microscope for 6 consecutive days.

3.4 Results and Discussion

3.4.1 Characterization of Photosynthetic Growth Distribution

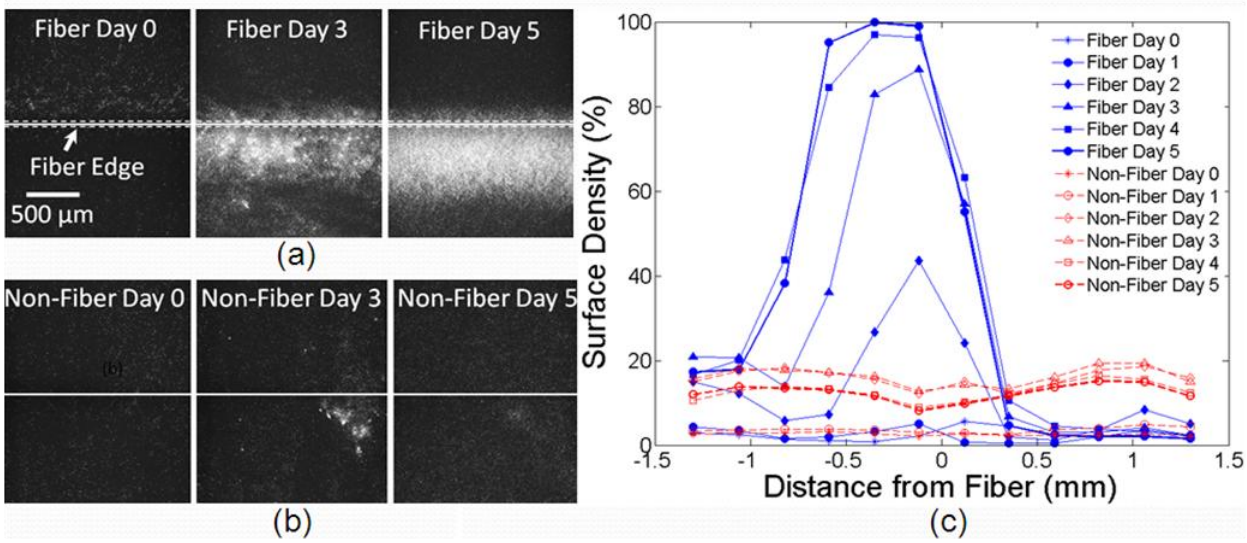

Figure 3.3 Cross-section of bacterial distribution perpendicular to fiber direction in light exposed reactors. Bacteria distribution in the middle of two sample reactors (imaged from the top): (a) the bacteria organize into a dense layer close to the fiber in fiber-equipped reactors (note fiber not seen as images are aligned to the fiber's edge), (b) in non-fiber reactors the bacteria take on a random distribution. (c) Quantitative representation of change in the cross-sectional surface density for the two sample reactors with time (distance is from center axis of the chip for the non-fiber reactor). The data points are averages across the total length of the observed region.

Photosynthetic growth of S. elongatus adjacent to a single HFM delivering CO_2 is reported here (Figure 3.3 (a)). Following inoculation, *S. elongatus* randomly settled on the bottom of the reactor. After 2 days, a more concentrated band of growth formed close to the fiber. This layer continued to expand throughout the fifth day of the experiment. While the initial distribution in the fiber and non-fiber reactors began

similarly, they diverged on day 2 with the bacteria distributing into a random pattern and ceasing to grow in the fiber-less reactor (Figure 3.3 (b)). To observe the increased growth adjacent to the entire length of the fiber, we averaged the local cross-sectional distributions together (Figure 3.3 (c)). The trends for the average cross-section distributions are the same as those presented for the local distributions shown in the images of the bacteria. This growth area corresponds to the dimensions over which the HFM can provide effective passive gas exchange for sustained growth. The bacteria in the initial distribution are in a monolayer in both the fiber and non-fiber reactors. In the high surface density layers that develop in the fiber-equipped reactors the bacteria are present in a multilayer. In the non-fiber reactor the bacteria remain in a low surface density monolayer.

In the light, fiber equipped reactors outgrew non-fiber controls by 3.3, 3.4 and 2.7 times for 6.0%, 2.5% and 0.35% surface densities respectively (p-value < 0.05) (Figure 3.4(a)). Increasing the initial *S. elongatus* concentration from 0.35% to 2.5% lead to a higher final surface density; however, a further increase from 2.5% to 6.0% did not significantly change the final surface density. This suggests that surface density saturation around a single fiber was reached after 5 days with a 2.5% starting inoculation under our experimental conditions. Dark controls (Figure 3.4(b)) demonstrate the level of surface coverage in these reactors attributed to bacterial settling and carryover growth from the preculture. At each inoculation concentration, an increase in surface coverage of about 5 fold was observed in the dark. This increase in the dark reactors was independent of presence of a fiber but is significantly lower than the growth in the illuminated fiber reactors.

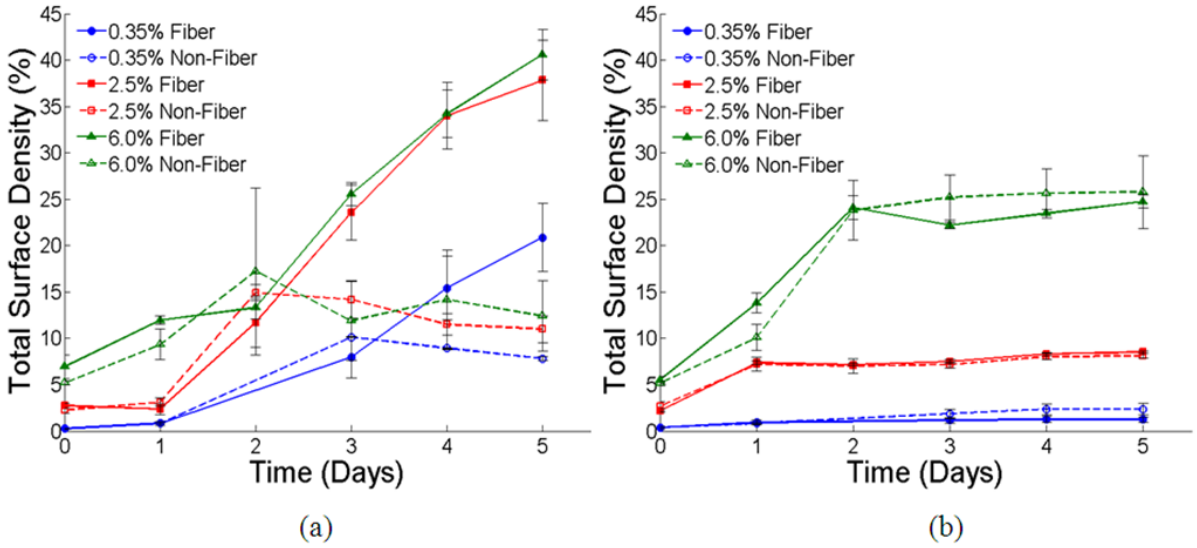

Figure 3.4 Total surface density with respect to time: The percent of area covered with bacteria was measured on a daily basis. (a) When exposed to light the reactors equipped with fibers outperformed the non-fiber reactors and grew continuously over the observation period. This trend was illustrated with images of these reactors in Figure 2. (b) In the dark, the difference between fiber and fiber-less reactors was negligible. For the reactors kept in the dark the increase in bacterial surface density was attributed to gravity driven settling of bacteria and carryover growth. Error bars represent the standard error of the mean.

The final average cross-sectional distributions showed distinct shapes depending on whether a fiber is present (Figure 3.5 (a)). In reactors without fibers, the distribution was essentially uniform and slightly higher in the case of the higher inoculations. The reactors with fibers, however, were not uniform in their growth patterns and included regions in which very high surface densities were achieved (close to 100% for the 2.5% and 6.0% surface densities). This is evidence of a dense photosynthetically active layer forming next to the fiber. Surprisingly, the distribution of this layer was consistently observed to not be symmetric with respect to the fiber position, and instead peaks slightly to one side of the fiber. Whether the peak is on the right or left side of the fiber varies reactor to reactor, but invariably a dense bacterial

layer developed along one side of the fiber. We have chosen to label the side of the fiber with this layer as the negative side in each reactor so that they can be directly compared. This asymmetry could have resulted from a bias in the initial distribution during the inoculation of the reactors; however, this bias is not clearly deduced from the data. The possibility that this was due the fact the cover-slip and the glass slide (forming the "roof" and "floor") are misaligned and affect the light distribution was considered. However, the misalignment occurs in all 3-axes and measurement of this imperfection across the reactors shows that the worst case deviation is 1mm over the 24 mm width of the cover slip, which corresponds to a maximum deviation angle of ~2.5°. Such a small imperfection should not affect the light distribution significantly enough to suppress growth completely on one side of the fiber. Furthermore, in reactors filled with standard BG-11 media, in which a carbon source is present, the bacteria distributions are uniform with respect to the fiber.

3.4.2 Analysis and Discussion

The presence of a fiber enhanced photosynthetic growth and facilitated formation of a high surface density bacterial layer adjacent to the fiber (Figure 3.4 and Figure 3.5 (a)). The region of enhanced growth can be quantified as the increase in surface density in the fiber-equipped reactors compared to the uniform surface density in the non-fiber and dark reactors. The area of enhanced growth per unit fiber length was found to be 1.7 ± 0.2 mm, 1.6 ± 0.1 mm, and 1.2 ± 0.2 mm for the 6.0%, 2.5% and 0.35% inoculations, respectively (Figure 3.5 (b)).

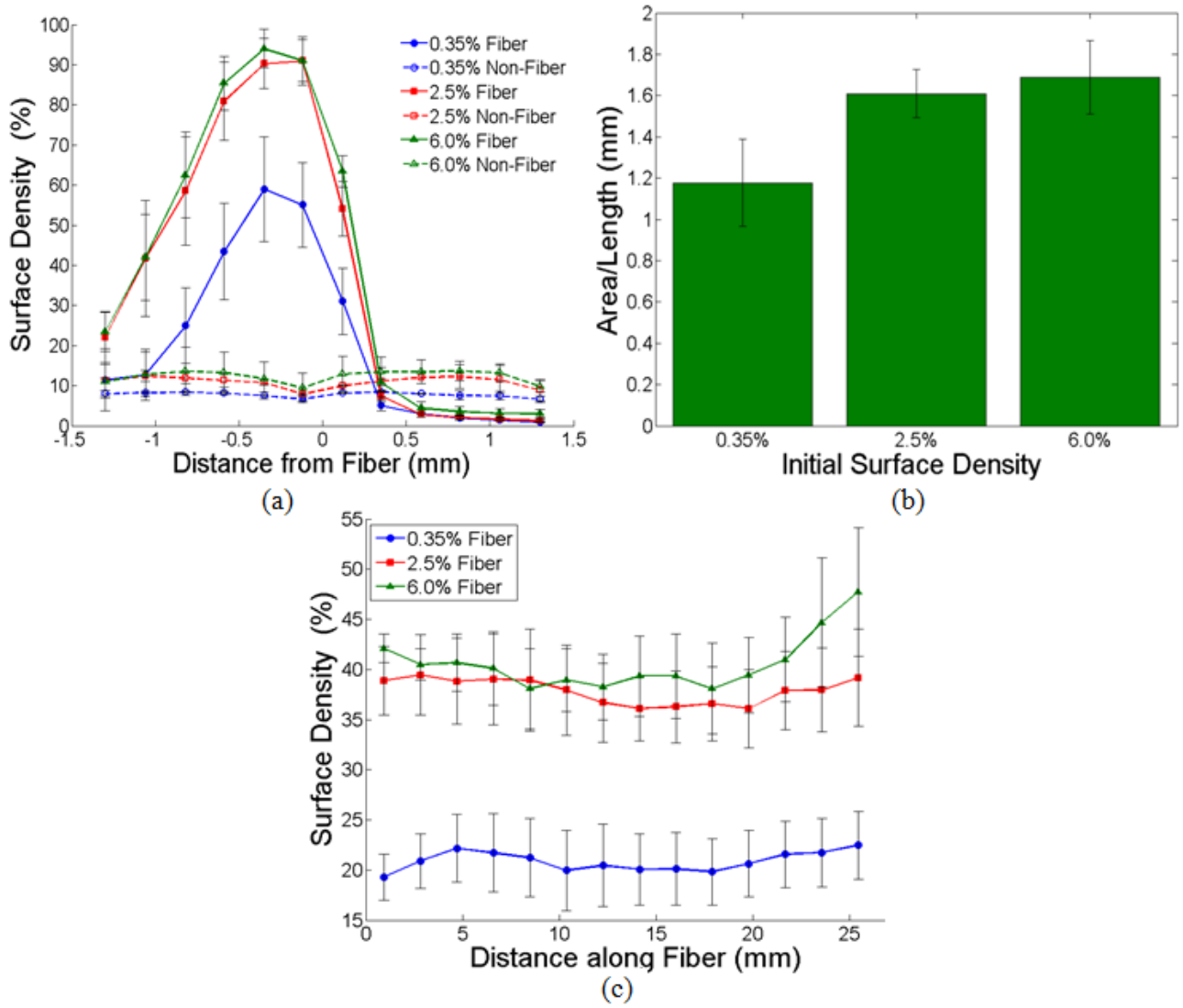

Figure 3.5 Final bacterial distribution after 5 elapsed days (observed region is 26 mm by 2.8 mm centered on fiber): (a) The comparison of the final cross-sectional distributions for the fiber and non-fiber reactors indicates that a region of enhanced growth develops on one side of the fiber. (b) The size of enhanced growth region is quantified as an area per length of fiber in which such growth occurs. (c) The lengthwise distribution does not exhibit a strong trend in the fiber reactors and serves to confirm that the cross-sectional distributions shown here persist for the length of the observed region. Error bars represent the standard error of the mean.

This corresponds to approximately 6, 5.5, and 4 fiber diameters. Increasing the initial surface density from 2.5% to 6.0% did not significantly change the range of the enhanced growth region indicating this result is close to the maximum that could be obtained from a single fiber. Since the diffusion of CO_2 perpendicular to the fiber depends on the partial pressure of CO_2 inside the fiber, the metrics obtained in this experiment only pertain to fibers supplied with atmospheric partial pressure of CO_2. The values for areas of enhanced growth per unit length fiber obtained here can be used to estimate the spacing between fibers that could be used in such a setup. To further show that the cross-sectional data presented is valid over the entire length of the fiber we investigated, we present the lengthwise bacteria distributions in Figure 3.5 (c). The variation in the distribution along this axis is within the experimental variability for the cases of the 0.35% and 2.5% initial surface density inoculation with a slight gradient noticeable for the 6.0% case. Any gradient in the lengthwise bacteria distributions would be indicative of a gradient in the partial pressure of CO_2 along the fiber, because, in CO_2 limited growth conditions the growth rate of the bacteria is proportional to the available CO_2 concentration. We observed variations only in the high initial inoculation case (where any changes variation of growth rate along the fiber would be magnified as compared to a lower initial inoculation), which leads us to posit that a close to uniform partial pressure of CO_2 was maintained throughout the entire length of the fiber. In every case, however, the variation in the lengthwise distribution is much less extreme than the variation in the cross-sectional distribution. This is consistent with the fact that the rate of gas transport through the fiber core should encounter less resistance than the rate of transport across the membrane of the

fiber and into the liquid phase. Because the length of fiber used in our experiments was only 2.6 cm, a much larger fiber would be needed to support a full scale PBR. With increasing fiber length, a more pronounced variation in the lengthwise partial pressure of CO_2 in the fibers would be expected if only passive transport is provided. However, this limitation could be overcome by active transport of carbon rich gas through the fiber.

In our work, we focused on characterizing growth in the micro-environment adjacent to a single HFM delivering CO_2 in an otherwise carbon starved environment. To compare the observed growth in our miniature reactors to growth in a traditional lab-scale growth chamber, specific growth rates were used as a metric. The specific growth rates in our experiments were calculated by fitting the surface density adjacent to the HFM versus time for each trial. Data for days 1-4 was used for this fit, as this was the observed exponential growth phase (Figure 3.4(a)). Different specific growth rates were observed to occur with different inoculation concentrations used. The results of these calculations are presented in Table 3.1 and are compared to the growth rate of *S. Elongatus* observed in bubble-aerated, continuously rapidly mixed, culture flasks maintained at a temperature of 35°C and a similar light flux (50 $\mu E\ s^{-1}\ m^{-2}$) as used in our experiments [27]. Though our miniature reactors operated in CO_2 limited conditions with no active transport methods, the growth rate observed in reactors started at a 0.35% initial surface density was 72% of the observed rate in a traditional laboratory scale reactor.

***S.Elongatus* Reactors**	**Specific Growth Rate μ (h^{-1})**	**Reactor Volume (mL)**
Lab-Scale *S.Elongatus* Growth Chamber	~0.0577	120
Our system - Initial Surface Density 0.35%	0.0415 ± 0.0097	4
Our system - Initial Surface Density 2.5%	0.0376 ± 0.0045	4
Our system - Initial Surface Density 6.0%	0.0158 ± 0.0025	4
Recent HFM Reactors		
Membrane-sparged helical tubular photobioreactor (MSTR)[24]	0.0190[a]	800
Hollow fiber membrane photo-bioreactor (HFMPB)[26]	0.0085[b]	500
Membrane carbonation photobioreactor (MCPBR)[25]	0.0083	5500

Table 3.1 Comparison of Specific Growth Rates. ([a]Estimated from plot, [b]Calculated from reported biomass productivity rate.)

Recent HFM studies have concentrated on incorporating HFM modules into PBR systems to enhance biomass production by improving CO_2 exchange, regulating pH, and promoting CO_2 fixation. However, the application of the HFMs has thus far only been investigated for their CO_2 delivery to bulk reactor volumes in recirculated PBRs. Table 3.1 shows specific growth rates from our experiments compared to results previously reported for PBRs utilizing integrated HFM modules, note that since the reactors operate under varying conditions and utilize different strains these numbers should not be used for an absolute comparison. Placed alongside values reported from previous HFM experiments the calculated growth rates from our experiments were of a similar magnitude. This analysis implies that, although demonstrated on only a small scale, the growth rates achieved in the micro-environment surrounding the fiber are comparable with other HFM reactors and with traditional bubble-aerated laboratory setups. It is also important to note that our system operated with no circulation.

Adding circulation, as in previous systems, increases mass transfer but impact cost considerations for a scaled up system. Light delivery challenges in a scaled up version could be overcome by using the slab-waveguide system we have previously developed [17].

3.5 Conclusion

In this work, we characterized the ability of a single HFM fiber to enhance the growth of *S. elongatus* in a simple batch reactor with no media circulation. The diffusive transport of atmospheric gas through a single HFM fiber and into the bacteria resulted in the development and sustained growth of a dense bacterial layer along the length of the fiber. We observed this effect over the length of a short fiber distance, but this same effect could potentially be produced by longer fibers after switching to an active rather than passive system of gas transport. This implies that the system should be readily scalable and this conjecture can be tested in future experiments. In conjunction with waveguide provided light, this system could serve as the backbone to a scalable PBR, harboring direct fuel-producing photosynthetic bacteria, operating at high volumetric productivities.

3.6 Acknowledgements

This work was supported by the academic venture fund of the David R. Atkinson Center for Sustainable Future and a CAREER grant from the National Science Foundation (NSF) for Optofluidics – Fusing Microfluidics and Photonics (#0846489).

The authors would also like to thank the James Liao group at UCLA for providing the *S. elongatus* strain used in this study. We also thank Matthew Mancuso for helpful discussions regarding the experiment and data analysis.

REFERENCES

1. Sheridan, C., *Making green.* Nature Biotechnology, 2009. **27**(12): p. 1074-1076.
2. Brennan, L. and P. Owende, *Biofuels from microalgae-A review of technologies for production, processing, and extractions of biofuels and co-products.* Renewable & Sustainable Energy Reviews, 2010. **14**(2): p. 557-577.
3. Searchinger, T., et al., *Use of US croplands for biofuels increases greenhouse gases through emissions from land-use change.* Science, 2008. **319**(5867): p. 1238-1240.
4. Fargione, J., et al., *Land clearing and the biofuel carbon debt.* Science, 2008. **319**(5867): p. 1235-1238.
5. Chisti, Y., *Biodiesel from microalgae.* Biotechnology Advances, 2007. **25**(3): p. 294-306.
6. Sharma, Y.C., B. Singh, and J. Korstad, *A critical review on recent methods used for economically viable and eco-friendly development of microalgae as a potential feedstock for synthesis of biodiesel.* Green Chemistry, 2011. **13**(11): p. 2993-3006.
7. Ghirardi, M.L., et al., *Hydrogenases and hydrogen photoproduction in oxygenic photosynthetic organisms*, in *Annual Review of Plant Biology*2007. p. 71-91.
8. McNeely, K., et al., *Redirecting Reductant Flux into Hydrogen Production via Metabolic Engineering of Fermentative Carbon Metabolism in a*

Cyanobacterium. Applied and Environmental Microbiology, 2010. **76**(15): p. 5032-5038.

9. Deng, M.D. and J.R. Coleman, *Ethanol synthesis by genetic engineering in cyanobacteria.* Applied and Environmental Microbiology, 1999. **65**(2): p. 523-528.
10. Luo, D.X., et al., *Life Cycle Energy and Greenhouse Gas Emissions for an Ethanol Production Process Based on Blue-Green Algae.* Environmental Science & Technology, 2010. **44**(22): p. 8670-8677.
11. Atsumi, S., W. Higashide, and J.C. Liao, *Direct photosynthetic recycling of carbon dioxide to isobutyraldehyde.* Nature Biotechnology, 2009. **27**(12): p. 1177-U142.
12. Ducat, D.C., J.C. Way, and P.A. Silver, *Engineering cyanobacteria to generate high-value products.* Trends in Biotechnology, 2011. **29**(2): p. 95-103.
13. Sheehan, J., *Engineering direct conversion of CO(2) to biofuel.* Nature Biotechnology, 2009. **27**(12): p. 1128-1129.
14. Aitken, D. and B. Antizar-Ladislao, *Achieving a Green Solution: Limitations and Focus Points for Sustainable Algal Fuels.* Energies, 2012. **5**(5): p. 1613-1647.
15. Jorquera, O., et al., *Comparative energy life-cycle analyses of microalgal biomass production in open ponds and photobioreactors.* Bioresource Technology, 2010. **101**(4): p. 1406-1413.
16. Xu, L., et al., *Microalgal bioreactors: Challenges and opportunities.* Engineering in Life Sciences, 2009. **9**(3): p. 178-189.

17. Jung, E.E., et al., *Slab waveguide photobioreactors for microalgae based biofuel production.* Lab on a Chip, 2012. **12**(19): p. 3740-3745.

18. Kumar, A., et al., *Enhanced CO(2) fixation and biofuel production via microalgae: recent developments and future directions.* Trends in Biotechnology, 2010. **28**(7): p. 371-380.

19. Carvalho, A.P. and F.X. Malcata, *Transfer of carbon dioxide within cultures of microalgae: Plain bubbling versus hollow-fiber modules.* Biotechnology Progress, 2001. **17**(2): p. 265-272.

20. Lin, H.J., et al., *Membrane Bioreactors for Industrial Wastewater Treatment: A Critical Review.* Critical Reviews in Environmental Science and Technology, 2012. **42**(7): p. 677-740.

21. Ahmed, F.N. and C.Q. Lan, *Treatment of landfill leachate using membrane bioreactors: A review.* Desalination, 2012. **287**: p. 41-54.

22. Gabelman, A. and S.T. Hwang, *Hollow fiber membrane contactors.* Journal of Membrane Science, 1999. **159**(1-2): p. 61-106.

23. Fan, L.H., et al., *Optimization of carbon dioxide fixation by Chlorelia vulgaris cultivated in a membrane-photobioreactor.* Chemical Engineering & Technology, 2007. **30**(8): p. 1094-1099.

24. Fan, L.-H., et al., *Evaluation of a membrane-sparged helical tubular photobioreactor for carbon dioxide biofixation by Chlorella vulgaris.* Journal of Membrane Science, 2008. **325**(1): p. 336-345.

25. Kim, H.W., et al., *Advanced Control for Photoautotrophic Growth and CO(2)-Utilization Efficiency Using a Membrane Carbonation Photobioreactor (MCPBR).* Environmental Science & Technology, 2011. **45**(11): p. 5032-5038.

26. Kumar, A., et al., *A hollow fiber membrane photo-bioreactor for CO(2) sequestration from combustion gas coupled with wastewater treatment: A process engineering approach.* Journal of Chemical Technology and Biotechnology, 2010. **85**(3): p. 387-394.

27. MacKenzie, T.D.B., R.A. Burns, and D.A. Campbell, *Carbon status constrains light acclimation in the cyanobacterium Synechococcus elongatus.* Plant Physiology, 2004. **136**(2): p. 3301-3312.

CHAPTER 4

HOLLOW FIBRE MEMBRANE ARRAYS FOR CO_2 DELIVERY IN MICROALGAE PHOTOBIOREACTORS

4.1 Abstract

Microalgae can serve as a carbon sink for CO_2 sequestration and as a feedstock for liquid fuel production. Methods for microalgal biomass and biofuel cultivation have to be developed, but are limited in the efficiency of light delivery and gas exchange within cultures. One method by which gas exchange within photobioreactors can be improved is through the use of hollow fibre membranes which enable simultaneous transport of gases deep into the reactor and rapid exchange with the culture media. Here we demonstrate the optimal geometric and operational conditions for CO_2 transport to planar cultures of photosynthetic organisms via hollow fibre membrane arrays. Specifically we investigate the effects inter-fibre spacing and active/passive aeration on the organism growth rate, planar surface density, and total biomass accumulation. We show that spacing larger than 3 times the fibre diameter lead to significant variations in the surface density and spatially resolved growth rate, whereas at around this spacing culture densities nearing 90% can be maintained for 17 days without decrease. Active aeration was shown to increase the specific growth rate and the average surface density by approximately 15% and 35%, respectively, while also eliminating gradients in the growth rate along the length of the fibres.

---

*Reprinted by permission of the Royal Society of Chemistry with permission from Michael Kalontarov, Devin F. R. Doud, Erica E. Jung, Largus T. Angenent and David Erickson "Hollow fiber membrane arrays for CO_2 in microalgae photobioreactors". *Energy and Environmental Science*, 2014. Submitted© RSC

4.2 Introduction

Concerns about the impact of climate change, CO_2 emissions, and energy security, have led to widespread interest in the production of biofuels from microalgae [1]. Microalgae have higher CO_2 fixation efficiencies and growth rates than other plant-based feedstocks [2, 3] and the potential to utilize waste-water or industrial gas wastes as nutrient sources [4]. The most developed method for extracting fuels from microalgae is converting their stored lipids into biodiesel [5], a process that is very energy intensive [6]. This has prompted the research and development of many engineered strains of bacteria to directly secrete fuels such as hydrogen [7, 8], ethanol [9, 10], isobutyraldehyde [11] and other high value products [12].

To take maximal advantage of these new strains, new photobioreactor (PBR) designs are required that can sustain high density cultures while enabling efficient light delivery and gas exchange [13]. The most common reactors used in algal cultivation are open raceway ponds and tubular-type enclosed reactors [14]. While these designs do have significant advantages [15], both are faced with fundamental limitations in delivery of sufficient light and CO_2 and extraction of products to maintain high photosynthesis rates [16]. The former of these problems has received a significant amount of attention as of late [17]. Uneven light distribution causes the culture to be overexposed at the surface and underexposed below the light penetration depth [18]. To counteract this problem many approaches have been investigated including the integration of optical fibres [19], interaction with evanescent [20] and plasmonic fields [21], and planar waveguides [22].

In parallel to the problem of light delivery, limitations in gas exchange and

transport are also being addressed. Traditionally, gas exchange in PBRs is provided by bubbling or passive exposure to the atmosphere [23]. Though easy to implement these methods constrain optimal PBR operation and possible culture densities. CO_2 delivery is limited by uneven distribution throughout the reactor volume [24]. Maintaining a uniform distribution is important for efficient volume utilization since regions with low CO_2 concentration suffer from lower rates of photosynthesis [25]. Turbulent flow mixing is a common mechanism by which CO_2 concentration is equilibrated. This condition require that a large amount of energy is spent on mixing the algal cultures [26], and contribute to the already high energy costs of the algal cultivation process [27]. This has motivated research into various methods for improving gas exchange coefficients in PBRs.

A recent advance in enhancing gas exchange has been the integration of hollow fibre membranes (HFMs) modules into PBRs [28]. A HFM consists of hollow fibres whose walls are membranes that allow for diffusive species exchange between the media inside and outside the fibre. They have been used in the chemical, petrochemical, pharmaceutical and galvanic industries [29], and applied in such varied applications as wastewater treatment [30], drinking water treatment [31], tissue engineering [32], and the development of artificial organs [33]. Recently, HFMs have shown potential to address the gas exchange challenges faced by PBRs [34, 35] and several lab scale reactors incorporating HFM modules have been reported [35-38]. These studies have verified the potential benefits of integration of HFMs into PBRs by reporting increased biomass production, improved gas exchange, regulation of pH, and promotion of CO_2 fixation. In previous work we have characterized the effectiveness

with which a single HFM fibre, applied independently of a module, can provide the necessary gas exchange to locally sustain growth in a carbon-limited reactor with no circulation and only passive gas transport[39].

Here we perform a study to determine the optimal operational and geometric conditions for the use of hollow fibre arrays as a method for delivery of CO_2 to planar cultures of photosynthetic organisms. We report on three experiments that investigate the effects of inter-fibre spacing and active/passive aeration on the organism growth rate, planar surface density, and total biomass accumulation. First, we have characterized what array spacing might be most effective by studying a two fibre unit cell. We then fabricated full HFM arrays and measured the behaviour of the organisms for an extended period of time (30 days). Lastly, a study characterizing the effect of adding active gas flow through the fibres was conducted

4.3 Materials and Methods

4.3.1 Investigation of Optimal Spacing

To characterize the effects of the spacing in a HFM fibre array we first conducted experiments on a unit cell of two fibres. Miniature reactors were fabricated, inoculated, and operated in the manner described in our previous work[39], however, as seen in Figure 4.1(a), two fibres were inserted instead of one. The dimensions of the sealed miniature reactors were 40 mm × 16 mm × 6 mm and the HFM fibres (model no. MHF304KM purchased from the Mitsubishi Rayon Co., Ltd.) were centered on the bottom of the reactors along the primary axis. The reactors consisted of an epoxy sealed PDMS chamber sandwiched between a microscope slide and a large cover slip

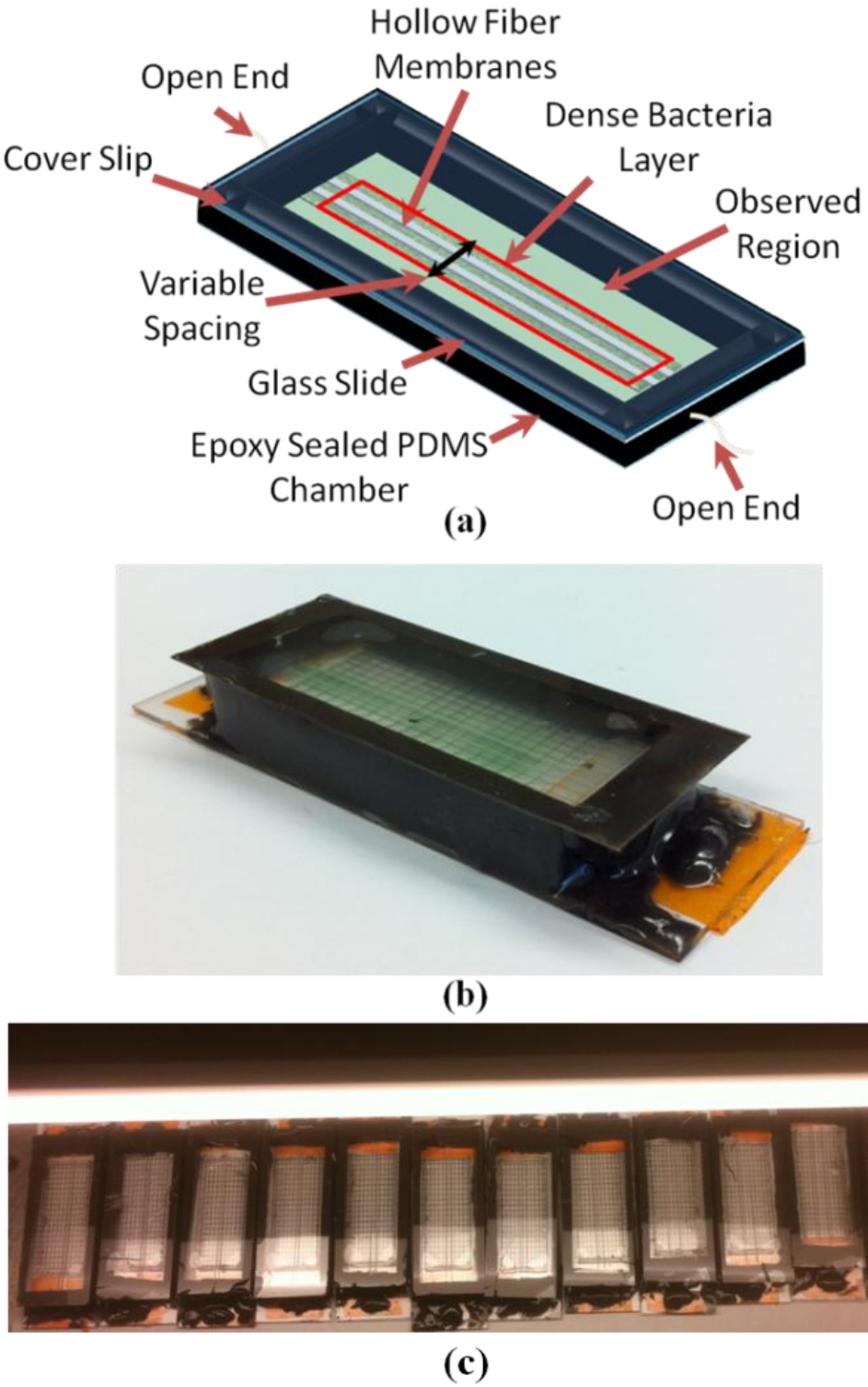

Figure 4.1 Two fibre unit cell miniature reactor: (a) Schematic of reactor (b) Picture of fully fabricated reactor (c) Reactors arranged under a fluorescent lamp.

(Figure 4.1 (a) and (b)). KwikWeld Epoxy (J-B Weld Company) was used as a sealant to make the reactors as gas tight as possible. The reactors were inoculated with *S. elongatus* SA665 (obtained from the Liao lab at UCLA[11]) and modified BG-11 media. The media was modified by the addition of a 50 mM phosphate buffer (pH 7.0), the removal of bicarbonate, and by sparging with N_2 for 30 min in an anaerobic serum bottle prior to re-suspension and inoculation of *S. elongatus*. This was done to make initial culture carbon source free and hence achieve CO_2 limited growth conditions in the reactor. The reactors were placed under two fluorescent lamp strips (American Fluorescent Plug-in Light Strip) which provided a photon flux density of 75 μE s^{-1} m^{-2} (Figure 1(c)). The ambient temperature in the laboratory was measured to be 25°C. The ends of the fibres where open to the atmosphere to allow passive gas exchange to occur through the fibres' lumens.

Three different unit cell spacing values were tested: 870 μm, 1740 μm, and 3480 μm. The diameter of the HFM fibres used here is ~290 μm, hence, these distance correspond to 3, 6, and 12 fibre diameters respectively. A 3D printed (OBJET Connex 500) frame was used to position the fibres on the glass slide and ensure the proper gap between them; epoxy was used to fix the fibres in place. Four reactors were fabricated for each spacing distance. The space between the fibres was imaged using fluorescence microscopy initially and seven days later. As can be seen in Figure 1(a), the observed region is offset from the edges of the reactor to minimize boundary effects on our measurement (the observed region was 26 mm long). The captured images were processed to map the surface density of bacteria distribution. Briefly, surface density is the percentage of the two-dimensional area, in this case between the

two fibres, that is covered by the bacteria (a more through description of imaging setup and processing algorithm is available in our previous publication[39]).

4.3.2 HFM Fibre Arrays

To conduct experiment with fibre arrays we fabricated larger reactors using the same processes as described above (Figure 4.2), except two large cover slides (75 mm × 50 mm × 1 mm) were used to sandwich the epoxy sealed PDMS chamber. The area of the reactor was increased to 58 mm × 38 mm × 6 mm. The fibre array was placed on the bottom of the reactor and centered; the fibres were arranged parallel to the long side of the reactor and were 75 mm in length. The fibre array spanned 20 mm and was offset from the walls of the reactor by about 1 cm on each side so that edge effects did not interfere with the growth in the array. The dimensions of the observed region were 20 mm × 40 mm, and the region was marked by a grid placed in the center of the reactor as seen in Figure 4.2(a). The grid served as a reference for imaging using a fluorescence microscope. The images were taken in the same manner as previously discussed. A total of 360 images were taken per reactor to map the bacteria distribution around fibre array. The images were stitched together to produce bacteria surface density maps. There were 3 reactors fabricated for each unit-cell type: 19 fibres were used to make the 3-diameter spacing array, and 11 fibres were used to make the 6-diameter spacing array, Figure 4.2(a). After being inoculated with bacteria (using same procedure as for the unit-cell experiments), the reactors were placed under the same fluorescent light strips as the previous experiment, Figure 4.2(b). The

experiment was conducted for 30 days and reactors were imaged daily for the first 6 days (Day 0 – Day 5), and again on Day 10, 17, and 30

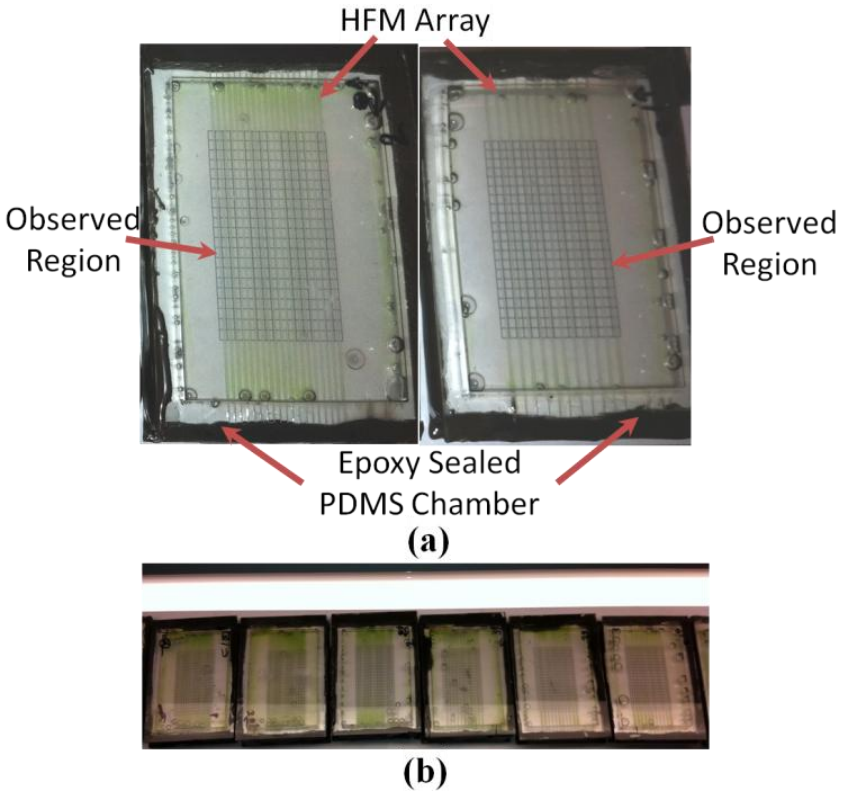

Figure 4.2 HFM Array Reactors: (a) Photographs of the two types of reactors tested: 3-diameter unit-cell (left) and 6-diameter unit-cell (right). (b) 3 reactors of each type were fabricated, and shown here arranged under the fluorescent lamp strip.

4.3.3 Active Gas Delivery

The goal of this experiment was to study the effect of active aeration on the growth of cyanobacteria in HFM array reactors; all other conditions such as the bacteria, media, light conditions, etc. were kept fixed compared to the previous experiment. To incorporate active flow into these reactors we built a setup which allows us to pump in compressed atmospheric air under controlled flow and pressure conditions; it is

illustrated in Figure 4.3. Three actively aerated reactors were compared to the same number of passively aerated and non-fibre control reactors. The concentration of CO_2 in the air provided to the passive and active reactors was at atmospheric levels. The actively aerated reactors were operated at a pressure of 0.5 psig, which corresponds to a flow rate of ~50mL/min. The reactors were of the same construction as used in the previous experiment except the fibre ends were bundled and inserted into a coupler to interface them with tubing. The fibres used in these experiments were approximately 10 cm long. The 3-fibre diameter spacing was chosen for the fibre array in these reactors. A centered 20 mm × 40 mm region was imaged on a daily basis using fluorescence microscopy in each reactor and analyzed with the previously described methods. Using these images the surface density of the bacteria in each reactor was calculated. The experiment was allowed to run for 5 days and upon completion the organisms were harvested from the reactors. Optical density measurements were conducted on these samples to compare final bacteria concentration achieved in the three different types of reactors.

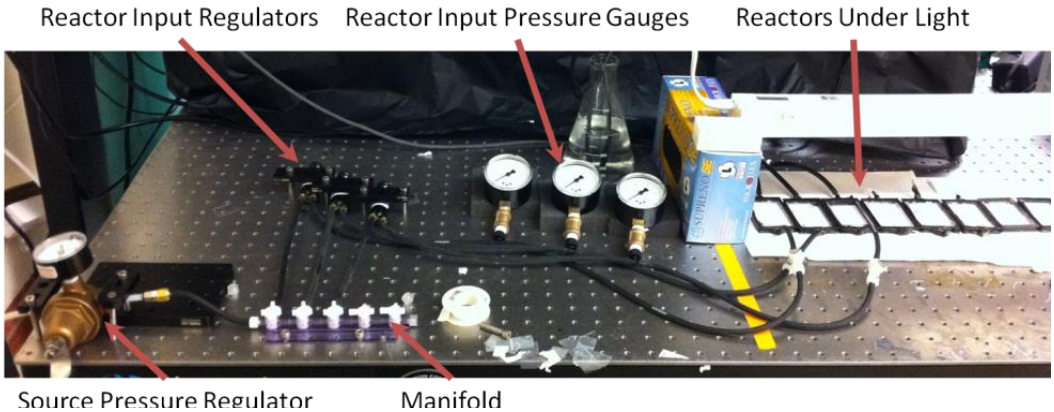

Figure 4.3 Setup for flow experiments: The setup consists of a compressed air source, manifold, and pressure regulators to allow for the active aeration of 3 miniature reactors. The actively aerated reactors are compared to 3 passively aerated reactors, and 3 control reactors with no fibres.

4.4 Results and Analysis

4.4.1 Investigation of Optimal Spacing

After seven days under light, the space between the fibres in each of the reactors was imaged and the average surface density was measured. Sample images of the inter-fibre spacing are presented in Figure 4.4 (a) and (b). The bacteria, which appear white in these fluorescence microscopy images, are initially at a low surface density (Day 1). By Day 7, the bacteria cover most of the available are except for a small gap. The local surface density measurements can be averaged together to get the surface density in the observed region for each reactor, with four reactors for each fibre spacing. The dependence of the surface density on the unit-cell fibre spacing is show in Figure 4.4(c). The surface density is highest for the 3-diameter spacing, reaching an average of 80%. The surface density decreased to 43% for a 6-diameter gap, and dropped to 24% for a 12-diameter gap. The amount of useable reactor surface area for each unit cell depends on the fibre spacing. For each unit-cell type the percentage of reactor area available for bacteria growth is 75%, 83%, and 92%, for the 3, 6, and 12-diameter gaps, respectively. Multiplying the respective measured surface densities and available area percentages yields the better comparison metric to identify which type of unit cell was more effective. This calculation yields adjusted surface densities (accounting for the reactor area taken up by the fibres themselves) of 60%, 36%, and 22% for the 3-, 6-, and 12-diameter gap unit-cells respectively. Based on these results we decided to further explore the 3-dimater and 6-diameter unit-cells by fabricating fibre arrays with these gaps.

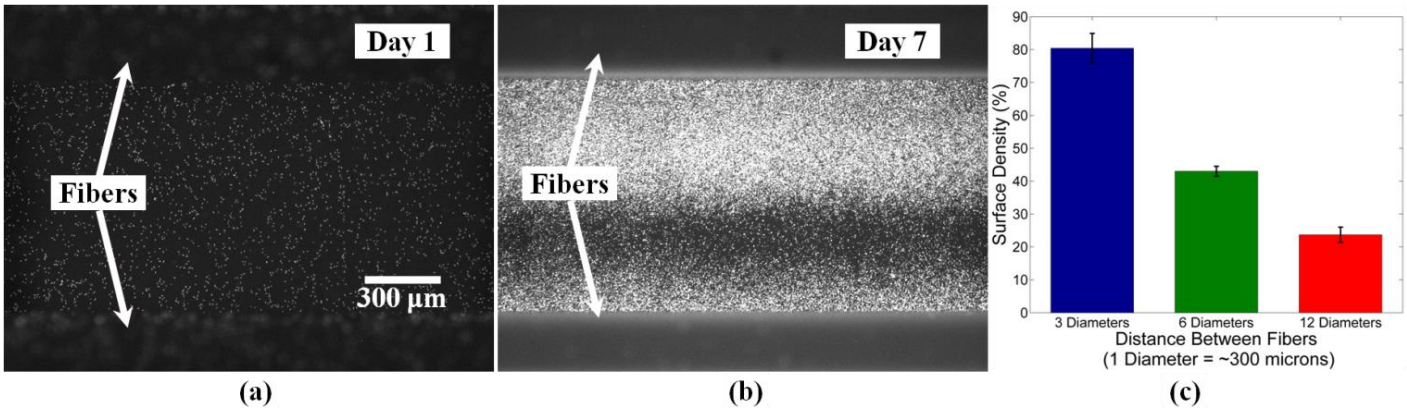

Figure 4.4 Final surface density for different unit cell fibre spacings: Example images of the space between fibres for a 3 diameter spacing on Day 1 (a) and Day 7 (b), illustrating the amount of area taken up by the bacteria on the initial and final days. (c) Comparison of the average surface density (averaged over the observed region) for the different unit-cell fibre spacings. Highest percentage reached with 3-diameter spacing

4.4.2 HFM Fibre Arrays

The bacteria distribution that developed in the two types of fibre arrays differed from each other both spatially and temporarily. In Figure 4.5, we present the surface density maps of the bacteria distribution on Day 0, 3, 5, 10, 16, and 30 for both array types. In both cases, the initial distribution is uniform and at a low surface density of 1.35% ± 0.4%. By Day 3, the surface density maps show clear evidence of bacteria growth and this growth is initiated next to the fibres for both cases. However, by Day 5 more of the area in the tighter spaced array is covered by bacteria than in the sparser array. Additionally, the quality of this coverage is also superior as the bacteria are at a higher surface density. By Day 10, most of the available area in the 3 fibre diameter spaced array is covered by a dense bacteria layer, however, in the 6 fibre diameter spaced array the bacteria are at a high surface density only in bands next to the fibres. The bacteria layer continues to get denser in the tighter array until the layer

completely covers all of the available area at an average surface density of 88%. In the sparser array the bacteria is limited to bands of high surface density next to the fibres. The measurements for Day 30 show that surface density of the bacteria distribution decreases in the center of the tighter array. For the sparser array, the bacteria bands next to the fibres expand slightly.

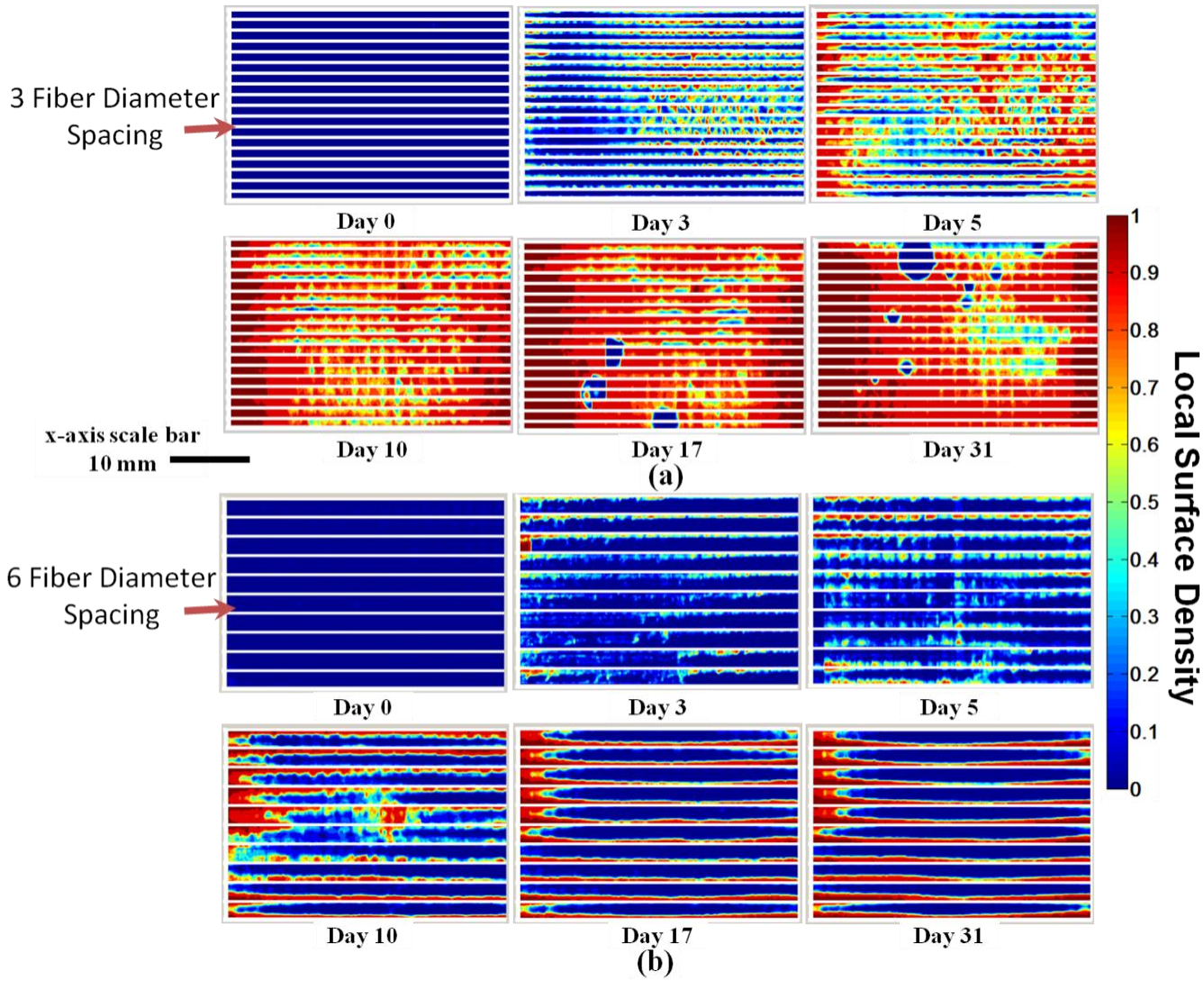

Figure 4.5 Surface density maps for two types of arrays over the course of 30 days: local surface density for the (a) 3 fibre diameter spaced array and (b) 6fibre diameter spaced array. A high density uniform bacteria layer develops in the tight fibre array, however, the bacteria grow in band next to the fibres in the sparse array.

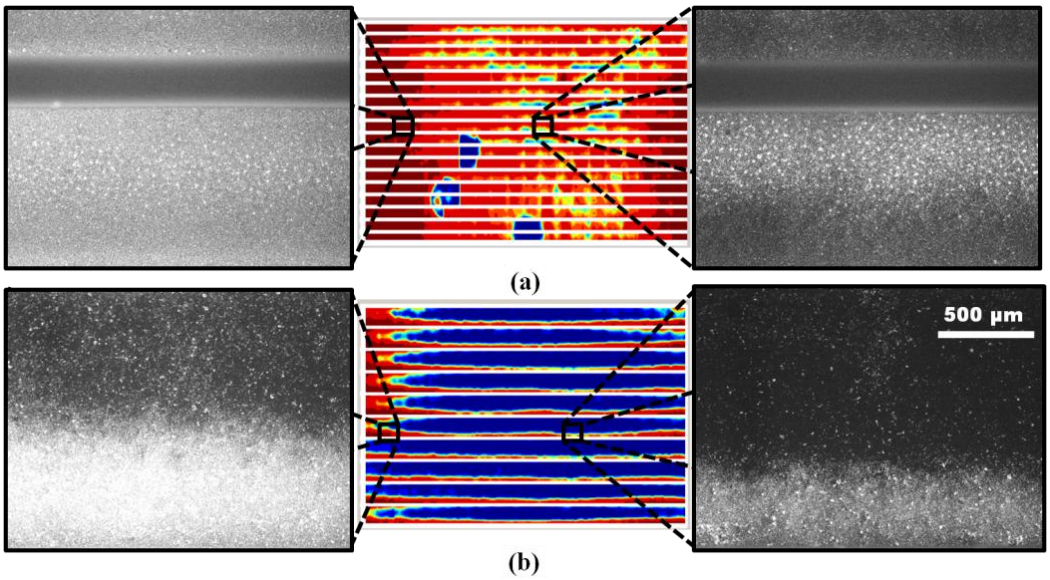

Figure 4.6 Micrographs of bacteria layers in HFM fibre array reactors. Images taken at the edge and center of the observed region in a 3 fibre diameter spaced reactor (a) and 6 fibre diameter spaced reactor.

To illustrate the bacteria layers, which we have so far represented by the surface density maps, we present several fluorescent microscopy images of the bacteria in these reactors in Figure 4.6. The surface density maps are made by processing multiple images and stitching the results together to map out the whole observed region in each reactor. Looking at the Day 17 map for the 3-fibre diameter spaced array (Figure 4.6(a)), very high surface density regions are seen on the left and right sides. The image in Figure 4.6(a) depicts what such a bacteria layer that formed in between the fibres looks like; note that there is minimal "black" (empty) space between the bacteria. The right image is taken at the center of the observed region and depicts a layer that has a lower local surface density region inside it. For the 6-fibre diameter spaced array (Figure 4.6(b)), we would like to illustrate how the size of the bacteria bands formed next to the fibre differs at two locations. On the left, the image depicts a

location closer to the observed region edge and a wider band of bacteria is seen. On the right, an image from the center is shown and here a thinner bacteria band is observed.

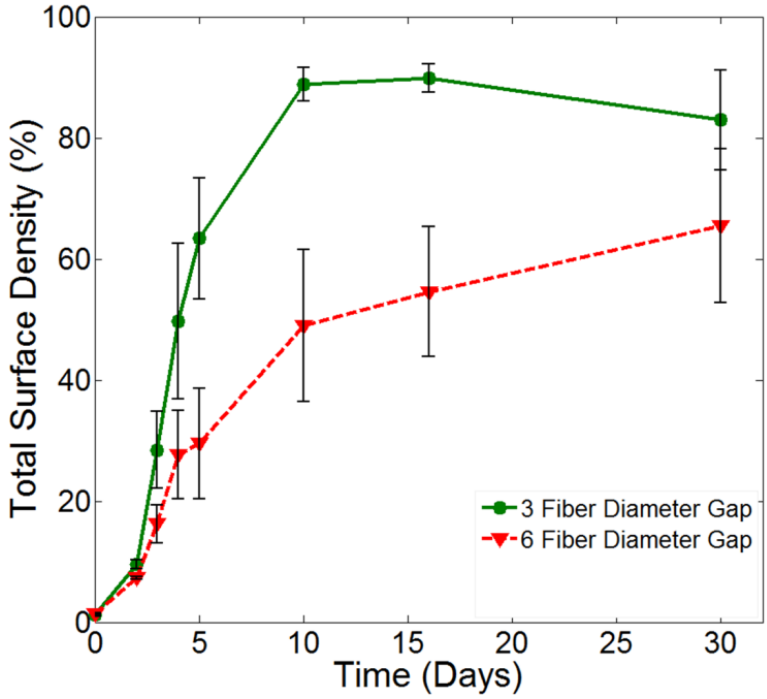

Figure 4.7 Total surface density in the observed region for the 3 fibre diameter spaced and 6 fibre diameter spaced reactors (n = 3 for each type). The error bars represent the standard error of the mean

In Figure 4.5, we illustrate the spatial variation in the bacteria distributions that developed in the two types of tested array designs. Data pertaining to the development of these distributions with respect to time is presented in Figure 4.7. This data describes the trends in the total surface density of the bacteria in the observed region for the complete set of reactors (n = 3 for each type). The total surface density is a representation of the fraction of the observed region coved by bacteria. Though the initial conditions for both types of reactors are virtually identical, the measured values for the surface density quickly diverge. In the reactors with tighter fibre arrays, a large

proportion of the available area becomes covered with bacteria in an exponential manner; after the 5 days 63% of the surface is coved by a bacteria layer. Growth is slower in the sparser array reactors and only 30% of the surface area is covered by the bacteria after 5 days. In the next phase, the rate at which the surface density grows decreases in both reactor types. The bacteria layers in the 3-fibre diameter spaced arrays reach a maximum average surface density of 88%. This high surface density persists until Day 17, but measurements made on Day 30 reveal that the density of these layers does not persists indefinitely and a decrease is observed. In reactors with 6-fibre diameter spaced arrays, the average surface density has been observed to increase at a slow rate through the course of the experiment.

By performing at exponential fit on the total surface density data for Days 0-4, we can obtain the specific growth rate for the bacteria layers that developed in these reactors. The average specific growth rate in the 3-fibre diameter spaced array and 6-fibre diameter spaced array reactors was found to be $0.041 \pm 0.004\ h^{-1}$ and $0.031 \pm 0.003\ h^{-1}$, respectively. We can also map the specific growth rate as a function of location in the observed region by applying the same method to the local surface density maps. Such maps are presented in Figure 4.8. When comparing the maps for the two types of arrays two trends are observed. In the tighter arrays the growth rates are distributed in a continuous manner, however, in the sparser array the areas of high growth rate are concentrated next to the fibres. This of course follows from the observations of the surface density maps presented earlier. Another trend is that in both cases the growth rates are higher closer to the edges of the observed region. This is an artifact of the fact that these reactors are passively aerated. CO_2 is entering the

reactors room the open ends on both sides of the reactors and only a depleted amount is able to arrive at the center thus limiting the growth there.

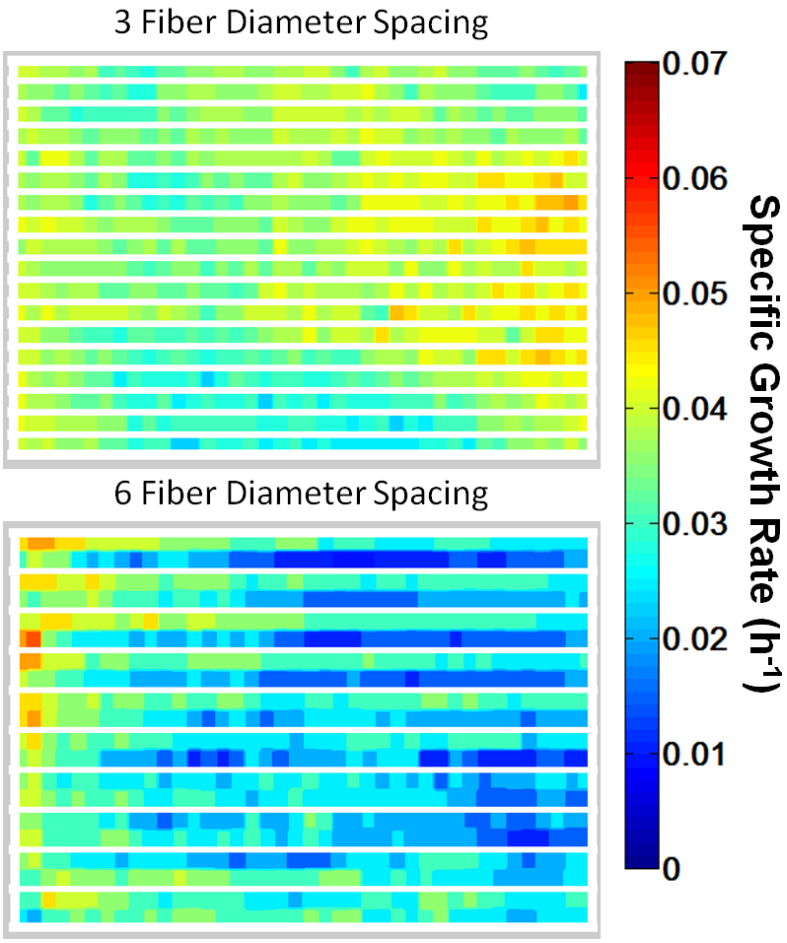

Figure 4.8 Local specific growth rate maps for the two types of fibre arrays with passive aeration. In the tighter array the growth rate distribution is more continuous than in the sparser array. Growth is also higher at the edges as expected for passive aeration

.

4.4.3 Active Aeration of HFM Array Reactors

In these experiments we compared how bacteria grew in actively aerated and passively aerated reactors with 3-fibre diameter spaced fibre arrays versus a set of control reactors without fibres. The total surface density of the observed regions for the complete set of reactors (n = 3 for each type) is plotted in Figure 4.9. The starting

density for this experiment was 3.0% ± 0.9%. The control reached the lowest surface density after 5 days (20%), due to being limited by gas transport through the liquid volume and exchange through the reactor walls. The passively aerated reactors behaved as before, exhibiting close to exponential growth and reaching 54% coverage during the course of the experiment. The actively aerated reactors reached 74%, the highest average surface density out of this set of reactors. The specific growth rates for the actively and passively reactors were calculated by performing an exponential fit on the total surface density data for the first four days. The average specific growth rates for the actively and passively reactors were 0.037 ± 0.002 h^{-1} and 0.032 ± 0.004 h^{-1}, respectively.

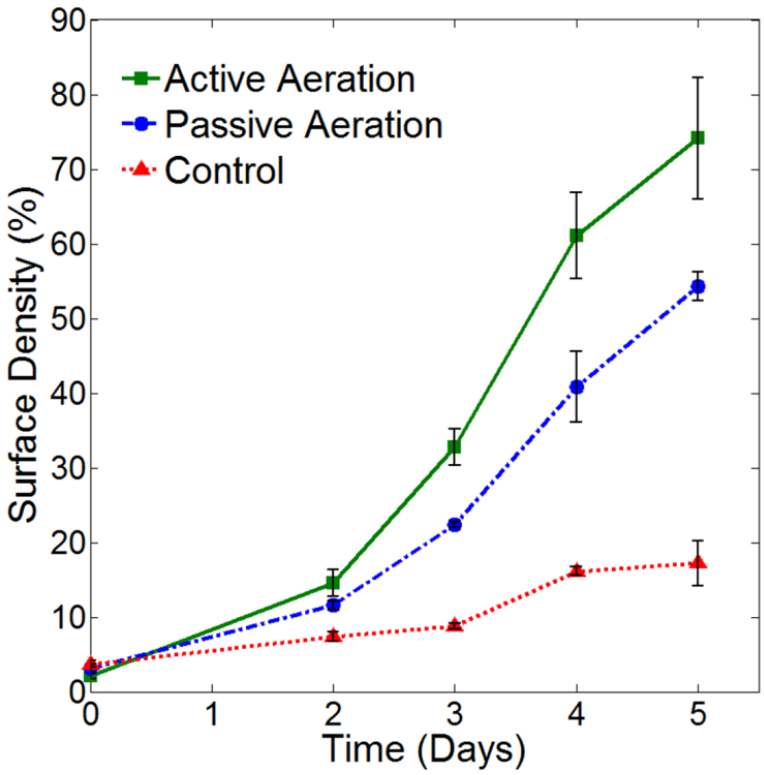

Figure 4.9 Total surface density in the observed region for the actively aerated, passively aerated, and control (non-fibre) reactors (n = 3 for each type). The error bars represent the standard error of the mean.

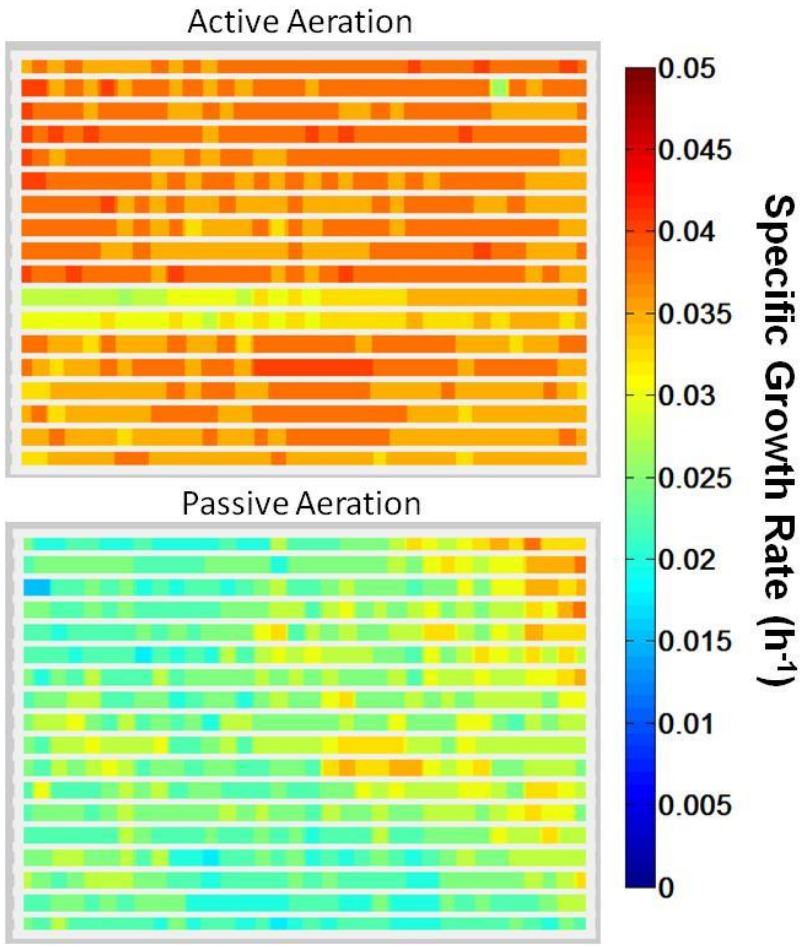

Figure 4.10 Local specific growth rate maps for reactors with active and passive aeration. In the actively aerated reactor the growth rate is more uniformly distributed along the length of the fibres. In the passively

We also present spatial distribution of the local specific growth rates for actively and passively aerated reactors in Figure 4.10. In the actively aerated reactor, the specific growth rate is uniformly distributed in the direction of gas propagation in the observed region. However, in the passively aerated reactor we see higher growth rates toward the left and right edges of the observed region. Finally, at the conclusion of the experiment we extracted the bacteria solution from the reactors and measured the optical density (OD) to compare the bacteria concentrations in these reactors. We

present this data in Figure 4.11. The initial OD for the experiment was 0. 05. The control reactors were found to have an OD of 0.05, due to growth at the edges of the reactors. In the passively aerated reactors, the OD of the bacteria solution reached 0.076 ± 0.008. The OD measurements for these two types of reactor are closer than the final surface density values, since the fibre array only covers ~53% of the available reactor area. The OD found in the aerated reactors was 0.214 ± 0.010. The surface density values for the actively and passively aerated reactors were much closer together due to the fact that even though in both types of reactors the bacteria layers covered a similar amount of area, the bacteria layer in the actively contained a larger number of bacteria due to being stacked to a larger degree in the third dimension.

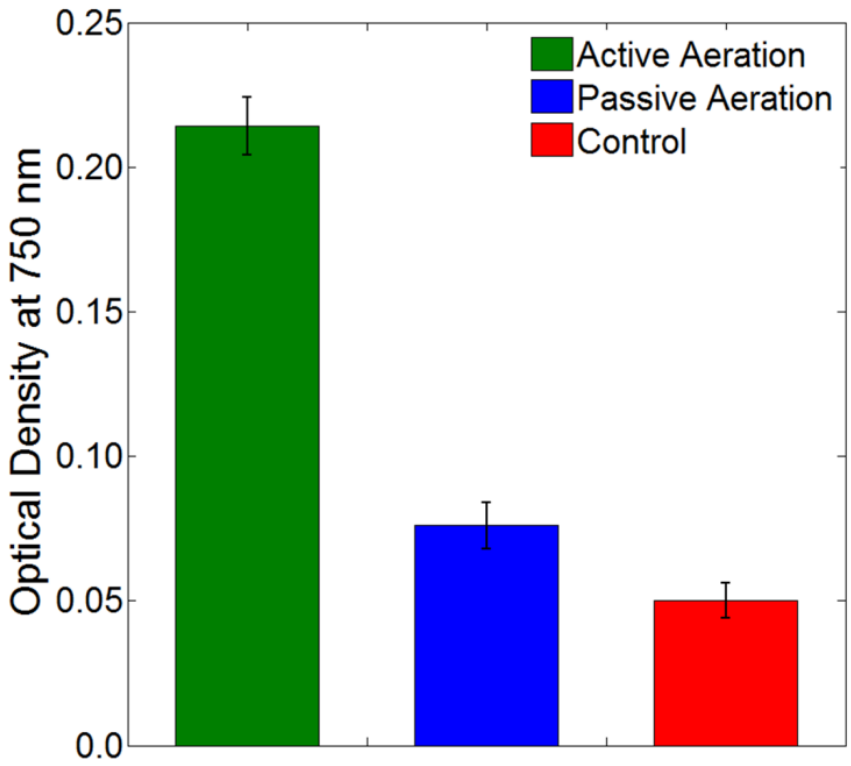

Figure 4.11 Optical density measurements of bacteria solution in actively aerated, passively aerated, and control reactors at the conclusion of the experiments.

4.5 Discussion

Reactor Type and Initial Surface Density	Specific Growth Rate μ (h^{-1}) (Days 0-4)	Final Surface Density (Day 5)
6 Fibre Diameter Spaced Array - Initial Surface Density 1.35%	0.0310 ± 0.003	30% ± 9%
3 Fibre Diameter Spaced Array - Initial Surface Density 1.35%	0.0410 ± 0.004	63% ± 10%
Passively Aerated Array - Initial Surface Density 3.0%.	0.0320 ± 0.004	54% ± 2%
Actively Aerated Array - Initial Surface Density 3.0%	0.0370 ± 0.002	74% ± 8%
Well Mixed Culture Flask [40]	0.0580	

Table 4.1 Comparison of Fibre Array Reactors.

Through the series of experiments whose results were presented above, we have shown that the localized effect of a single HFM fibre on bacteria growth could be extended to a large area by properly arraying multiple fibres. Table 4.1 allows us to compare the results of these experiments. For context, the *Elongatus* observed in a bubble-aerated, continuously rapidly mixed, culture flasks maintained at a temperature of 35°C and a similar light flux (50 μE s^{-1} m^{-2}) as used in our experiments was reported to be ~0.058 [40]. The growth rates observed in our experiments range from 53% - 71% of growth rate in well mixed culture flasks but was observed without any mixing. In the single fibre experiments, the growth rates observed depended on the initial surface density [39]. The same trend is seen in the array reactors, as the experiments started at 3.0% initial surface density have somewhat lower growth rates. For the same initial surface density, however, using the 3 fibre diameter spacing in the arrays increased the growth rate by 30% and more than doubled the surface density after 5 days with respect to the 6 fibre diameter array spacing. Additionally, our 30

day experiments with the 3 fibre diameter spaced array reactors show that the surface density of the bacteria layers increases even further after Day 5 and can be maintained at these high values without mixing or media replenishment for at least 17 days without drop off. The area spanned by the array in our experiments was 800 mm^2, but it could be indefinitely increased further if more fibres were added to the array and still deliver the same performance. By properly spatially arranging the fibres we were able to achieve the goals of distributing CO_2 and providing channels for gas transport throughout a PBR over any area.

The caveat to the previous statement is that though the width of the area over which the fibres need to be applied could be unlimited, the length would be constrained by the length of the fibres themselves. If passive aeration is used the fibre length is limited by gradients in the CO_2 concentration along the fibre. The effects of this constraint can be observed in the specific growth rate maps for the passively aerated reactors which were presented in Figures 4.8 and 4.10. In both those cases the "hot" spots for growth were close to the edges of the observed region. Over the length tested in out reactors, 7.5 cm – 10 cm, the growth in middle was diminished but still allowed for a uniform distribution of bacteria to develop over time, as seen in Figure 4.5. If longer fibres were used the gradients in bacteria growth rates would increase, potentially to the point that growth in the centre would be inhibited. To mitigate this problem we have considered actively aerating the reactors. When compared to passively aerated reactors in the same experiment, active aeration improved the initial specific growth rate and the final average surface density by approximately 15% and 35%, respectively (Table 4.1). Furthermore, a more uniform distribution in the growth

rate was observed (Figure 4.10); no discernible gradients along the fibre direction indicate that active aeration is a way to overcome this constraint on length. The uniformity of the distribution could be maintained for any fibre length as long as the flow rate, input gas CO_2 concentration, and desired bacteria concentration are properly matched. The proper combinations of these conditions will be explored in future experiments. Lastly, OD measurements revealed that adding aeration also greatly increased the amount of bacteria in the layers that developed around the fibres by providing better access to CO_2 than passive aeration, as indicated by the 3 times greater final OD in the actively aerated reactors.

4.6 Conclusions

In this work we have directly applied HFM fibres to provide gas exchange and facilitate bacteria growth without circulation or media replenishment. We have done this by utilizing fibre arrays. In our first experiments we tested array spacings of 3, 6, and 12 fibre diameters to narrow down the design space. We determined that the 3 and 6 fibre diameter spaced unit-cells performed better since the final surface density in for those cases were 2.7 and 1.6 times better than the 12 fibre diameter case respectively. We then built fibre arrays with those dimensions that spanned across approximately 20 mm. The 3 fibre diameter arrays outperformed the 6 fibre diameter arrays by 30% in terms of initial growth rate and by 100% with respect to the surface density on Day 5. Furthermore, an average surface density of 88% was maintained in these reactors for at least 17 days. Adding active aeration increased the growth rate

and surface density as compared to a passively aerated reactor. In reactors with active aeration, gradients in the growth rate were observed to decrease. Measurements of the optical density at the conclusion of the experiment also revealed a 3 times greater bacteria concentration in the actively aerated reactors. In summary, fibre arrays have been demonstrated as a possible way to provide gas exchange and facilitate uniform growth over any surface area.

4.7 Acknowledgements

This work was supported by the Advance Research Project Agency – Energy and the academic venture fund of the David R. Atkinson Center for Sustainable Future. The authors would also like to thank the James Liao group at UCLA for providing the S. elongatus strain used in this study. We also thank Matthew Mancuso for helpful discussions regarding the experiment and data analysis.

REFERENCES

1. Lam, M.K., K.T. Lee, and A.R. Mohamed, *Current status and challenges on microalgae-based carbon capture.* International Journal of Greenhouse Gas Control, 2012. **10**: p. 456-469.
2. Williams, P.J.L., *Biofuel: microalgae cut the social and ecological costs.* Nature, 2007. **450**(7169): p. 478-478.
3. Fargione, J., et al., *Land clearing and the biofuel carbon debt.* Science, 2008. **319**(5867): p. 1235-1238.
4. Brennan, L. and P. Owende, *Biofuels from microalgae-A review of technologies for production, processing, and extractions of biofuels and co-products.* Renewable & Sustainable Energy Reviews, 2010. **14**(2): p. 557-577.
5. Stephenson, A.L., et al., *Life-Cycle Assessment of Potential Algal Biodiesel Production in the United Kingdom: A Comparison of Raceways and Air-Lift Tubular Bioreactors.* Energy & Fuels, 2010. **24**: p. 4062-4077.
6. Sander, K. and G.S. Murthy, *Life cycle analysis of algae biodiesel.* International Journal of Life Cycle Assessment, 2010. **15**(7): p. 704-714.
7. Ghirardi, M.L., et al., *Hydrogenases and hydrogen photoproduction in oxygenic photosynthetic organisms*, in *Annual Review of Plant Biology*2007. p. 71-91.
8. McNeely, K., et al., *Redirecting Reductant Flux into Hydrogen Production via Metabolic Engineering of Fermentative Carbon Metabolism in a Cyanobacterium.* Applied and Environmental Microbiology, 2010. **76**(15): p. 5032-5038.

9. Deng, M.D. and J.R. Coleman, *Ethanol synthesis by genetic engineering in cyanobacteria.* Applied and Environmental Microbiology, 1999. **65**(2): p. 523-528.

10. Luo, D.X., et al., *Life Cycle Energy and Greenhouse Gas Emissions for an Ethanol Production Process Based on Blue-Green Algae.* Environmental Science & Technology, 2010. **44**(22): p. 8670-8677.

11. Atsumi, S., W. Higashide, and J.C. Liao, *Direct photosynthetic recycling of carbon dioxide to isobutyraldehyde.* Nature Biotechnology, 2009. **27**(12): p. 1177-U142.

12. Ducat, D.C., J.C. Way, and P.A. Silver, *Engineering cyanobacteria to generate high-value products.* Trends in Biotechnology, 2011. **29**(2): p. 95-103.

13. Erickson, D., D. Sinton, and D. Psaltis, *Optofluidics for energy applications.* Nature Photonics, 2011. **5**(10): p. 583-590.

14. Aitken, D. and B. Antizar-Ladislao, *Achieving a Green Solution: Limitations and Focus Points for Sustainable Algal Fuels.* Energies, 2012. **5**(5): p. 1613-1647.

15. Jorquera, O., et al., *Comparative energy life-cycle analyses of microalgal biomass production in open ponds and photobioreactors.* Bioresource Technology, 2010. **101**(4): p. 1406-1413.

16. Xu, L., et al., *Microalgal bioreactors: Challenges and opportunities.* Engineering in Life Sciences, 2009. **9**(3): p. 178-189.

17. Williams, P.J.L. and L.M.L. Laurens, *Microalgae as biodiesel & biomass feedstocks: Review & analysis of the biochemistry, energetics & economics.* Energy & Environmental Science, 2010. **3**(5): p. 554-590.

18. Lee, C.G., *Calculation of light penetration depth in photobioreactors.* Biotechnol. Bioprocess Eng., 1999. **4**: p. 78-81.

19. Chen, C.Y., et al., *Phototrophic hydrogen production in photobioreactors coupled with solar-energy-excited optical fibers.* International Journal of Hydrogen Energy, 2008. **33**(23): p. 6886-6895.

20. Ooms, M.D., et al., *Evanescent photosynthesis: exciting cyanobacteria in a surface-confined light field.* Physical Chemistry Chemical Physics, 2012. **14**(14): p. 4817-4823.

21. Ooms, M.D., L. Bajin, and D. Sinton, *Culturing photosynthetic bacteria through surface plasmon resonance.* Applied Physics Letters, 2012. **101**(25).

22. Jung, E.E., et al., *Slab waveguide photobioreactors for microalgae based biofuel production.* Lab on a Chip, 2012. **12**(19): p. 3740-3745.

23. Kumar, A., et al., *Enhanced CO(2) fixation and biofuel production via microalgae: recent developments and future directions.* Trends in Biotechnology, 2010. **28**(7): p. 371-380.

24. Carvalho, A.P. and F.X. Malcata, *Transfer of carbon dioxide within cultures of microalgae: Plain bubbling versus hollow-fiber modules.* Biotechnology Progress, 2001. **17**(2): p. 265-272.

25. Sanchez, G.B., M; Rodriguez, F; Sevilla, FJM; Alias, BC; Fernandez, AFC., *Minimization of carbon losses in pilot-scale outdoor photobioreactors by model-based predictive control.* Biotechnol Bioeng., 2003. **84**(5): p. 532-43

26. Beal, C.M., et al., *The Energy Return on Investment for Algal Biocrude: Results for a Research Production Facility.* Bioenergy Research, 2012. **5**(2): p. 341-362.

27. Chisti, Y., *Response to Reijnders: Do biofuels from microalgae beat biofuels from terrestrial plants?* Trends in Biotechnology, 2008. **26**(7): p. 351-352.

28. Abd Rahaman, M.S., et al., *A review of carbon dioxide capture and utilization by membrane integrated microalgal cultivation processes.* Renewable & Sustainable Energy Reviews, 2011. **15**(8): p. 4002-4012.

29. Pabby, A.K. and A.M. Sastre, *State-of-the-art review on hollow fibre contactor technology and membrane-based extraction processes.* Journal of Membrane Science, 2013. **430**: p. 263-303.

30. Agrahari, G.K., et al., *Removal of dissolved H2S from wastewater using hollow fiber membrane contactor: Experimental and mathematical analysis.* Desalination, 2013. **314**: p. 34-42.

31. De Souza, N.P. and O.D. Basu, *Comparative analysis of physical cleaning operations for fouling control of hollow fiber membranes in drinking water treatment.* Journal of Membrane Science, 2013. **436**: p. 28-35.

32. Mohebbi-Kalhori, D., et al., *Computational modeling of adherent cell growth in a hollow-fiber membrane bioreactor for large-scale 3-D bone tissue engineering.* Journal of Artificial Organs, 2012. **15**(3): p. 250-265.

33. Palakkan, A.A., et al., *Evaluation of Polypropylene Hollow-Fiber Prototype Bioreactor for Bioartificial Liver.* Tissue Engineering Part A, 2013. **19**(9-10): p. 1056-1066.

34. Gabelman, A. and S.T. Hwang, *Hollow fiber membrane contactors.* Journal of Membrane Science, 1999. **159**(1-2): p. 61-106.

35. Fan, L.H., et al., *Optimization of carbon dioxide fixation by Chlorelia vulgaris cultivated in a membrane-photobioreactor.* Chemical Engineering & Technology, 2007. **30**(8): p. 1094-1099.

36. Fan, L.-H., et al., *Evaluation of a membrane-sparged helical tubular photobioreactor for carbon dioxide biofixation by Chlorella vulgaris.* Journal of Membrane Science, 2008. **325**(1): p. 336-345.

37. Kim, H.W., et al., *Advanced Control for Photoautotrophic Growth and CO(2)-Utilization Efficiency Using a Membrane Carbonation Photobioreactor (MCPBR).* Environmental Science & Technology, 2011. **45**(11): p. 5032-5038.

38. Kumar, A., et al., *A hollow fiber membrane photo-bioreactor for CO(2) sequestration from combustion gas coupled with wastewater treatment: A process engineering approach.* Journal of Chemical Technology and Biotechnology, 2010. **85**(3): p. 387-394.

39. Kalontarov, M., et al., *In situ hollow fiber membrane facilitated CO2 delivery to a cyanobacterium for enhanced productivity.* RSC Advances, 2013. **3**: p. 13203-13209.

40. MacKenzie, T.D.B., R.A. Burns, and D.A. Campbell, *Carbon status constrains light acclimation in the cyanobacterium Synechococcus elongatus.* Plant Physiology, 2004. **136**(2): p. 3301-3312.

CHAPTER 5

CONCLUSIONS

In this dissertation, I presented a research on the topics of 3D fluidic assembly and the use of hollow fiber membranes to enhance gas exchange in photobioreactors.

5.1 Summary of accomplishments and future directions

5.1.1 Hydrodynamically driven docking of blocks for 3d fluidic assembly

In this chapter, I presented results that increased our understanding of the interactions that occur at one docking site during 3D fluidic assembly.

- Characterized the behavior of blocks as they are attracted to a docking site by fluid flow using numerical simulations and showed that blocks whose rotational motion was constrained achieved better alignment with the docking site.
- Experimentally demonstrated alignment parallel with the docking site in 97% of trials using blocks with an unbalanced mass distribution to limit their rotational degrees of freedom.
- Demonstrated the ability to assemble a single free floating block to a fixed substrate using a three dimensional flow field for cm-scale blocks.
- Experimentally characterized alignment efficiency of 3 block surface designs.
- Optimized flow conditions for successful docking.

- Experimentally demonstrated successful docking, i.e. fully aligned docking, at a rate of 54%

Our system has demonstrated the ability of 3D fluidic assembly to operate on the cm-scale. This is useful for the assembly of macroscale objects with a reasonable resolution. The next steps would be to demonstrate the assembly, reconfiguration, and disassembly of multi-block structures by valving the channels in the blocks. I have conducted preliminary work toward this goal. By having only the channel aligned with the blocks' self-orientation axis open (the vertical axis) multi-block structure could be assembled by stacking. In a series of proof of concept experiments I was able to demonstrate the assembly of three blocks in a vertical and horizontal configuration. In future work the system can be further optimized to demonstrate reconfiguration. Integration of on block components, such as active valves, sensors, etc. could increase the functionality of the system. Work along this direction has been conducted in the Cornell Creative Machines Lab over the last several years.

5.1.2 In situ *hollow fiber membrane facilitated CO_2 delivery to a cyanobacterium for enhanced productivity*

In this chapter, I demonstrated the effectiveness characterized the effectiveness with which a single HFM fibre can provide the necessary gas exchange to locally sustain growth in a carbon-limited reactor with no circulation and only passive gas transport.

- Experimentally determined that a single fiber enabling passive transport from/to the atmosphere can provide enough gas exchange to increase biomass accumulation by > 2.5 times with respect to a non-fiber control.
- Observed growth rate in the micro-environment next to the fiber was measured to be 72% of the observed rate in a traditional laboratory scale reactor for the same organisms and operating conditions However, our system operated without circulation or active gas delivery.
- The extent of the micro-environment around the fiber in which growth was enhanced was measured to span between 1.2 mm and 1.7 mm in the radial direction.

The data collected in these experiments was used as a starting point for our investigation of hollow fiber membrane arrays.

5.1.3 Hollow fiber membrane arrays for CO_2 delivery in microalgae photobioreactors.

In this chapter, I have demonstrated the optimal geometric and operational conditions for CO_2 transport to planar cultures of photosynthetic organisms via hollow fiber membrane arrays.

- Determined the optimum inter-fiber spacing to be 870 μm by conducting experiments with a two-fiber unit cell and full arrays.
- Demonstrated that in these arrays spacing culture densities nearing 90% can be attained and maintained for a time period of at least 17 days.

- Active aeration was shown to increase the specific growth rate and the average surface density by approximately 15% and 35%, respectively, while also eliminating gradients in the growth rate along the length of the fibers.
- Experimentally verified that hollow fiber membrane arrays are a possible way to provide gas exchange and facilitate uniform growth over any surface area.

The future work with this system will center on integrating it with the light delivery scheme that has been developed in parallel to my work. It is also important to further characterize the relationship between gas flow through the fibers and bacteria concentrations and growth rates. Toward this end I have collaborated on the construction of extensive laboratory setup in which many reactors can operated at different flow rates simultaneously. Finally, I have collaborated on preliminary experiments on product extraction using these fiber arrays and the initial results have been promising. Integration of all of these components would make a complete and novel photobioreactor system which can achieve higher volume efficiencies in terms of bacteria density and productivity than the state of the art.

5.1.4 Experimental parameter space to be explored in further work with fiber array reactors.

My work has been a first attempt to experimentally characterize the operation of HFM arrays as a method of gas exchange in planar photobioreactors. In further work a systematic investigation into the relationships between the many parameters that can influence the performance of this system should be analyzed to determine conditions

for optimal performance and any operational tradeoffs. The important independent variables to test are: light intensity, fiber spacing, fiber length, gas composition, gas flow rate, and initial bacteria concentration. The dependent variables to be measured include surface density maps, bacteria growth rate, bacteria concentration, and exhaust gas composition.

This is an extensive parameter space and eliminating certain variables could greatly help the experimental plan. Light intensity can be eliminated by setting it to a value in the optimal range for the organisms. Gas composition can be eliminated by setting it to the highest value the organisms can tolerate, or to a value constrained by economic factors. Fiber length could be varied only after the best conditions for the other variable are found since performance should only decrease with increasing length. This leaves fiber spacing, gas flow rate, and initial bacteria concentration as the independent variables. This three dimensional space can be explored on the reactor farm that has been developed by me and my colleagues.

5.2 Concluding Remarks

This dissertation has shown new directions in two fields: programmable matter and photobioreactor design for biofuel production. In the first part of this dissertation, I have numerically and experimentally characterized single block docking during 3D fluidic assembly, and in some part brought the futuristic idea of programmable matter close to reality. In the second part of this dissertation, I have demonstrated a way to

enhance gas exchange in photobioreactors using hollow fiber membrane array and contributed to a larger project toward creating better photobioreactors.